SATELLITE MEASUREMENTS OF HIGH LATITUDE CONVECTION ELECTRIC FIELDS

DAVID P. CAUFFMAN

and

DONALD A. GURNETT

Dept. of Physics and Astronomy, The University of Iowa, Iowa City, Ia., U.S.A.

(Received May, 1971; revision received December, 1971)

Abstract. This paper reviews the first results of satellite experiments to measure magnetospheric convection electric fields using the double-probe technique.The earliest successful measurements were made with the low-altitude (680–2530 km) polar orbiting Injun-5 spacecraft (launched August, 1968). The Injun-5 data are discussed in detail. The Injun-5 results are compared with the initial findings of the electric field experiment on the polar orbiting OGO-6 satellite (400–1100 km, launched June, 1969).

In addition to electric fields, the Injun-5 spacecraft also measures electric antenna impedance and thermal and energetic charged particle densities. Knowledge of these parameters makes possible a detailed investigation of the operation of the electric antenna system. We report on this investigation and discuss errors attributed to sunlight shadows on the probes, wake effects, and other factors. The Injun-5 experiment can generally determine electric fields to an accuracy of about ± 30 mV m^{-1}, and under favorable conditions, accuracies of ± 10 mV m^{-1} can be obtained.

Reversals in the electric field at auroral zone latitudes are the most significant convection electric field effect discovered in the Injun-5 data. Electric field magnitudes of typically 30 mV m^{-1}, and sometimes 100 mV m^{-1}, are associated with reversals. Electric field reversals occur on $\sim 36\%$ of auroral zone traversals, at about 70° to 80° invariant latitude, at all local times, and in both hemispheres. The latitude of a reversal often changes markedly on time scales less than 2 h. Electric potentials of greater than 40 keV are associated with these high latitude electric fields. Reversals occur at the boundary of measurable intensities of >45 keV electrons and are coincident with inverted 'V' type low energy electron precipitation events. In almost all cases the $\mathbf{E} \times \mathbf{B}/B^2$ plasma convection velocities associated with reversals are directed east or west, with anti-sunward components at higher latitudes and sunward components at lower latitudes. Maximum convection velocities are typically ~ 1.5 km s^{-1} and ordinarily occur at the auroral zone near the reversal.Two extreme (and many intermediate) configurations of anti-sunward plasma convection have been observed to occur on the high latitude side of electric field reversals: (1) Ordinarily, >0.75 km s^{-1} convection is limited to narrow ($\sim 5°$ INV wide) zones adjacent to the reversal. (2) For $\sim 14\%$ of reversals >0.75 km s^{-1} anti-sunward convection has been observed across the entire polar cap along the trajectory of the Injun-5 spacecraft. A summary pattern of >0.75 km s^{-1} polar thermal plasma convection is presented.

Electric field measurements from the OGO-6 satellite have substantiated many of the initial Injun-5 observations with improved accuracy and sensitivity. The OGO-6 detector revealed the persistent occurrence of anti-sunward convection across the polar cap region at velocities (<0.75 km s^{-1}) not generally detectable with the Injun-5 experiment. The OGO-6 observations also provided information indicating that the location of the electric field reversal shifts equatorward during periods of increased magnetic activity.

The implications of the electric field measurements for magnetospheric and auroral structure are summarized, and a list of specific recommendations for improving future experiments is presented.

1. Introduction

The importance of electric field measurements for studying the convection of plasma in the magnetosphere has been recognized for a number of years (Dungey, 1961;

Space Science Reviews **13** (1972) 369–410.

Axford and Hines, 1961; Piddington, 1962; Alfvèn, 1967; Bostrom, 1967). A review of theories of magnetospheric convection has been given by Axford (1969). Only recently have techniques for the measurement of magnetospheric electric fields been developed. These techniques include (1) observations of the drift of artificial barium clouds (Haerendel *et al.*, 1967; Foppl *et al.*, 1968; Mende, 1968; and Wescott *et al.*, 1969), (2) measurements of potential differences between Langmuir probes on rockets and satellites (Mozer and Bruston, 1967; Aggson, 1969; Fahleson *et al.*, 1970; Gurnett, 1970; Maynard and Heppner, 1970; Potter, 1970; and Cauffman and Gurnett, 1971a), (3) subionospheric electric field measurements with double probes carried by high altitude balloons (Mozer and Serlin, 1969), and (4) various other more indirect methods such as observations of whistler duct motions from spectral analysis of radio noise measurements (Carpenter, 1970), autocorrelation of backscattered signals of double radar pulses (Woodman and Hagfors, 1969), and simultaneous charged particle energy spectrum observations at different points in space (Van Allen, 1970). Electric 'field mill' devices (Wildman, 1965) have not yet proved practical in the magnetosphere. Measurements employing these various methods are compared in the reviews by Haerendel (1970), who discusses several additional untested techniques, and Maynard (1971), who gives a historical summary. Of all the methods, the most extensive and sensitive measurements have been obtained from artificial barium cloud releases, which have been reviewed by Haerendel and Lust (1970) and Haerendel (1970).

Satellite measurements provide much more extensive spatial coverage and quantities of data than is possible with either sounding rockets or barium cloud releases. Only in the past two years have results from satellite borne double-probe type electric field experiments become available. At the present time successful satellite double-probe electric field experiments have been flown on the Injun 5 satellite, launched in August, 1968, on the OGO-6 satellite, launched in June, 1969, and on the IMP-I satellite, launched in March, 1971.

The analysis of the Injun-5 electric field data is essentially complete. Results of this study for dawn and dusk local times have been reported in the literature (Cauffman and Gurnett, 1971a). OGO-6 data are still being analyzed. Data processing has just begun for the IMP-I experiment. Details pertinent to the electric field measurements made by these three spacecraft are shown in Table I. Electric field experiments have also been flown on OV1-17 and 18, OV1-21S, and SSS-A, for which no analyzed data are yet available.

This paper reviews the first results of these satellite experiments. The operation and results of the electric field experiment on the low altitude polar orbiting Injun-5 satellite are discussed in detail. Currently available OGO-6 results (J. P. Heppner, T. L. Aggson, and N. C. Maynard, private communications; J. P. Heppner, paper presented at IUGG (Moscow), August 1971) are also discussed. In particular, electric field phenomena which persist for long times ($\geqslant$ hours) are studied and interpreted in terms of magnetospheric thermal plasma convection. A summary of the implications of the electric field measurements for magnetospheric and auroral structure is

TABLE I

Satellite DC electric field experiments

	Spacecraft		
	Injun 5	OGO 6	IMP I
Launch date	August 8, 1968	June 6, 1969	March 13, 1971
Apogee	2530 km	1600 km	32.4 R_E
Perigee	680 km	400 km	240 km
Inclination	81°	82°	29°
Orbital period	118^m	120^m	100^h
Spin period	10^m to 6^h*	not spinning	12^s
Spin axis orientation	$\parallel$ **B***		$\perp$ ecliptic
Stabilization	geomagnetic field	3-axis inertial	inertial spin
Probe type	spheres	cylinders	cylinders
Active Probe dimension	20.3 cm diam.	4.5 m long	23 m long
Number of dipoles	1	1	2
Dipole baseline	2.85 m	18.4 m	69 m
Dipole orientation	$\perp$ **B***	Horizontal and $\perp$ **S**	$\perp$ spin (in ecliptic)
Principal investigator	D. Gurnett	T. Aggson	T. Aggson
Laboratory	U. of Iowa	NASA/GSFC	NASA/GSFC
Duration of data coverage	30 months (still operating)	13 days**	2 months (still operating)
Local times	all	dawn-dusk**	all

* After alignment ($\pm 15°$) with the geomagnetic field (Dec. 3, 1968).
** Operable in Earth's umbra (midnight local times) through June 20, 1971.

given, and specific recommendations are made for improving future experiments to measure convection electric fields.

2. Instrumentation

A. THE INJUN-5 ELECTRIC FIELD EXPERIMENT

The electric field sensors on Injun 5 consist of two spherical aluminum probes separated by 2.85 m between centers, along an axis parallel to the spacecraft y axis. A high impedance (~ 20 MΩ) differential amplifier determines the potential difference between the electric field probes. The average AC impedance of the two spheres is measured by differentially driving the spheres with a constant amplitude 30 Hz current source while measuring the AC potential difference between the spheres. As indicated in Figure 1, the spacecraft is oriented by an internal bar magnet such that the x axis of the spacecraft is maintained parallel to the geomagnetic field. The electric field experiment is therefore sensitive to a component of the electric field, $E_\perp$, perpendicular to the geomagnetic field. Details of the orbit of the Injun-5 satellite are given in Table I. Table II summarizes the parameters of the electric field experiment. For more information about the electric field experiment on Injun-5 see Gurnett *et al.* (1969). As discussed in Section 4, the absolute accuracy of the Injun-5 electric field experiment is generally about ± 30 mV m^{-1} and can be as good as

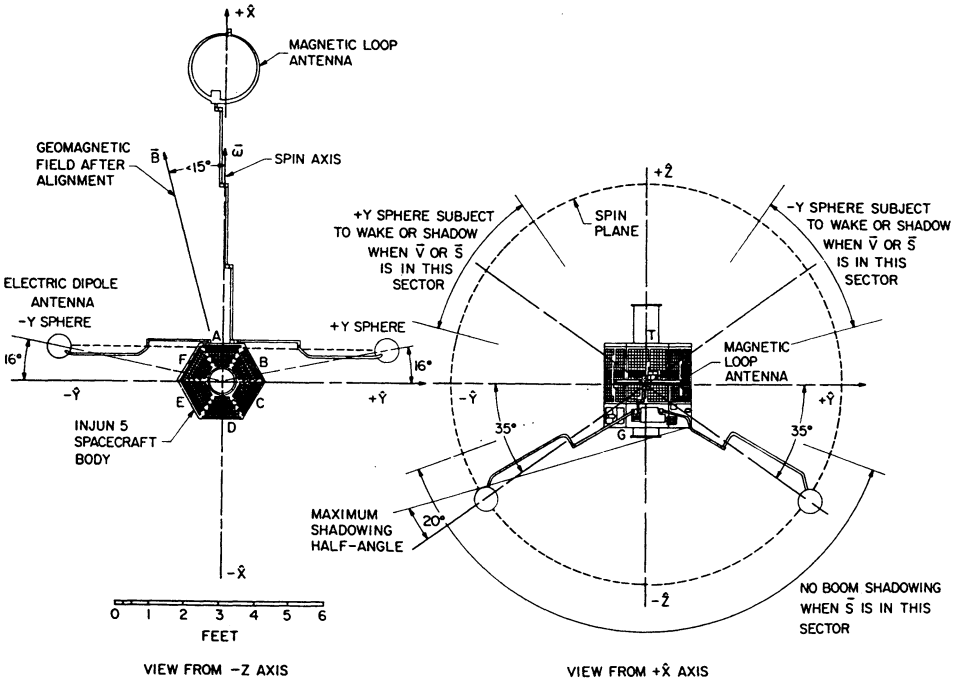

Fig. 1. Orientation of electric antennas on the Injun-5 satellite.

TABLE II

Parameters of the Injun-5 DC electric field experiment

Sphere separation distance	2.85 m between centers
radius	0.1015 m
coating	conducting silver paint with gold dots for thermal control
Boom coating	black insulating paint
diameter	0.019 m
Differential amplifier	
dynamic range	±1.0 V
RC time constant	0.4 s
input impedance to each sphere	20 MΩ
Electric field sampling rate	
normal data rate mode	every 4 s
high data rate mode	every 4/30 s
Tape recorder storage capacity (normal data rate only)	456 min of data
Impedance measurement	
frequency	30 Hz
sampling rate	every 30 s
constant current	0.1 μA rms

± 10 mV m^{-1} under certain favorable conditions. The resolution of the experiment is 2.75 mV m^{-1}.

B. THE OGO-6 ELECTRIC FIELD EXPERIMENT

The dipole electric antenna on OGO 6 consists of two cylindrical elements extended from either side of the spacecraft, with a separation distance of 18.4 m between the centers of the conductive elements. A differential amplifier with an input impedance of $\sim 10^{12}$ Ω monitors the potential difference between the elements once each second. The antenna ($\bar{X}$) axis is maintained nearly perpendicular to both the Sun-satellite and the Earth-satellite directions, as shown in Figure 2. At high latitudes OGO-6 therefore samples primarily one component of $E_{\perp}$.

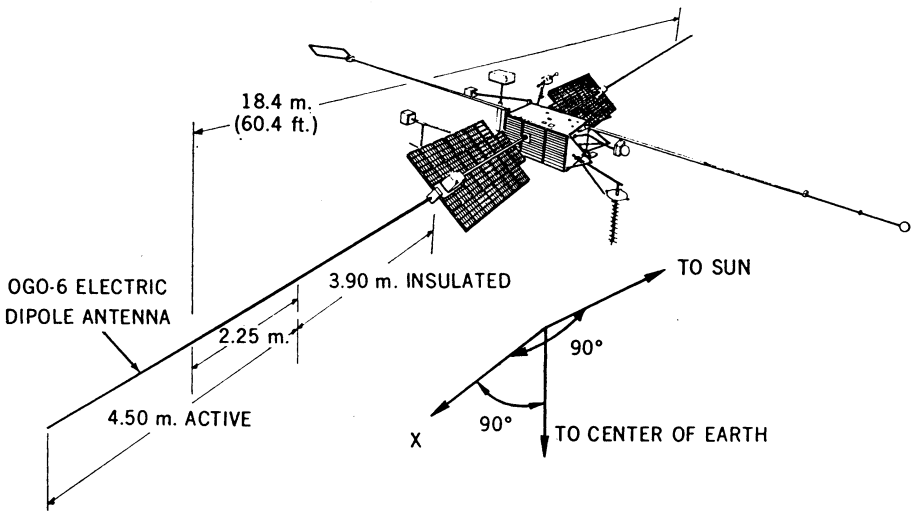

Fig. 2. Perspective view of the OGO-6 spacecraft, showing the cylindrical electric antennas, which are oriented perpendicular to the Sun direction and parallel to the horizon.

OGO-6 operated with nearly continuous data coverage for two weeks, until an internal short-circuit in the spacecraft power system occurred, limiting operation of the electric field experiment to times when the spacecraft is in the Earth's shadow. The OGO-6 data reported in this paper were taken during the initial two-week period, when the orbit was dusk-to-dawn over the northern hemisphere. Table I gives more details of the OGO-6 orbit and data coverage.

The orientation of the OGO-6 spacecraft precludes shadow effects on the electric antennas and the long boom length keeps the active portions of the cylinders beyond the effects of the satellite wake. Data analysis for the OGO-6 DC electric field experiment is therefore comparatively simple: subtraction of the $\mathbf{V}_s \times \mathbf{B}$ electric field component from the data yields the magnetospheric electric field. During the initial two weeks of data coverage the electric dipole axis was approximately aligned with

the satellite velocity vector, so the $\mathbf{V} \times \mathbf{B}$ field is small, of the order of the magnetospheric fields encountered. The absolute accuracy of the OGO-6 electric field experiment is believed to be between ± 5 and ± 10 mV m^{-1} from the combination of uncertainties in contact potentials and spacecraft attitude. The resolution of the experiment is about 1 mV m^{-1}.

3. Theory

A review of current theories of spacecraft interaction with the ionosphere has been given by Kasha (1969). The detailed theory of electric field measurements with symmetrical double probes on satellites has been discussed by Aggson and Heppner (1964), Aggson (1966), and Fahleson (1967). The rudiments of the theory are given here for later reference in discussing the observed operation in orbit.

The problem considered is that of two conductive probes moving in a plasma of high conductivity. The theory involved employs the approximations of (1) a Maxwellian two-component plasma, (2) ion velocity < spacecraft velocity $\ll$ electron velocity, and (3) small deviations of the probe potentials from neutrality. MKS units will be used. A high impedance probe immersed in a highly conducting plasma has four principal current constituents in its current-balance equation, $i = i_e - i_i - i_p$. The electron current to an arbitrary-shaped electrode, according to Langmuir theory (Mott-Smith and Langmuir, 1926), is given by

$$i_e = I_e e^{V/U_e} \quad \text{for} \quad V \leqslant 0, \tag{1a}$$

and we take

$$i_e = I_e \quad \text{for} \quad V \geqslant 0 \tag{1b}$$

in terms of parameters defined in Table III. The ion current to a moving probe is given approximately by

$$i_i = I_i \quad \text{(for any } V\text{)}. \tag{2a and 2b}$$

When the probe is in sunlight there will also be a photo-electron current which is assumed to be given by

$$i_p = I_p \quad \text{for} \quad V \leqslant 0, \tag{3a}$$

or

$$i_p = I_p e^{-V/U_p} \quad \text{for} \quad V \geqslant 0. \tag{3b}$$

The photo-electron current, I_p, depends only on the surface properties of the probe, and the exponential dependence in Equation (3b) is an empirical approximation for the energy distribution of the emitted photoelectrons (Aggson, 1966). Using the relations above, the current balance equation may be solved for the floating potential, V, defined as the probe potential when $i = 0$;

$$V = -U_e \ln [I_e/(I_i + I_p)] \quad \text{for} \quad V \leqslant 0 \tag{4a}$$

$$V = U_p \ln [I_p/(I_e - I_i)] \quad \text{for} \quad V \geqslant 0 \tag{4b}$$

TABLE III

Standard parameters used in probe model calculation

Symbol	Quantity	Value
T_e	electron temperature	2500 K
T_i	ion temperature	1500 K
n	number of density of ions or electrons	10^3 to 10^6 particles cm^{-3}
n_p	photo-electron number density	10^3 particles cm^{-3}
V_s	satellite velocity in a reference frame corotating with the earth	7 km s^{-1}
r	radius of sphere	0.1015 m
l	sphere separation	2.85 m
r_b	spacecraft body radius	0.305 m
E_y	maximum electric field component measured	350 mV m^{-1}
R_{B+}	bias resistance: $+y$ sphere branch	$2.0\times10^7\ \Omega$
R_{B-}	bias resistance: $-y$ sphere branch	$1.9\times10^7\ \Omega$
U_p	photo-electron potential kT_p/e	1.5 V
m_e	electron mass	9.11×10^{-31} kg
e	magnitude of electron charge	1.6×10^{-19} C
m_i	ion mass	16 amu; 2.7×10^{-26} kg
I_{p+}	photo-electron current to $+y$ sphere in sunlight	3×10^{-6} A
I_{p-}	photo-electron current to $-y$ sphere in sunlight	2×10^{-6} A
I_{pb}	photo-electron current to spacecraft body in sunlight	7.5×10^{-6} A
I_p	photo-electron currents in darkness or shadow	0.0 A
I_e	$=-4\pi r^2 ne\left(\frac{kT_e}{2\pi m_e}\right)$	
I_i	$=4\pi r^2 ne\left(\frac{kT_i}{2\pi m_i}+\frac{\lvert V_s\rvert^2}{16}\right)^{1/2}$	
U_e	$=kT_e/e$	

Zero potential has been defined to be the 'space' or 'plasma' potential. When a bias current I_B is applied to an electrode, the condition $I_B \leqslant I_e - I_i - I_p$ (or alternatively $I_B \geqslant I_e - I_i - I_p$) determines whether the probe voltage, V, will be negative (or positive) and whether Equations (1) through (4) part a (or part b) will hold. If the floating potential, V, is positive, an inhomogeneous 'photo-sheath' of electrons forms around the probe. If the floating potential, V, is negative, then the probe repels electrons and a 'positive ion sheath' forms around the probe. The thickness of the inhomogeneous

sheath which forms around the probes is characterized by the photo-sheath length

$$\lambda_p = (\varepsilon_0 U_p / n_p e)^{\frac{1}{2}} \qquad (V > 0)$$

in the case of a photo-electron sheath and by the Debye length

$$\lambda_D = (\varepsilon_0 U_e / ne)^{\frac{1}{2}} \qquad (V < 0)$$

in the case of a positive ion sheath.

Figure 3 shows a Thevenin equivalent circuit of the probe-plasma system for a plasma containing an electric field E_y parallel to the axis through the two probes (y axis). The voltage drops V_{s+} and V_{s-} across the sheaths of the electrodes are given

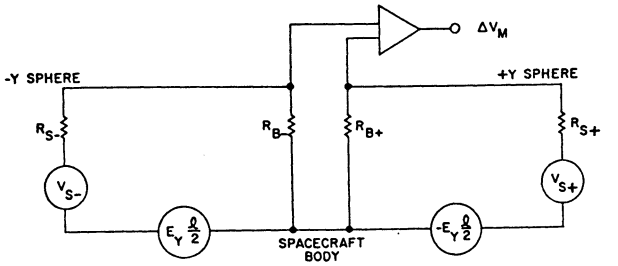

Fig. 3. Equivalent circuit of the probe-plasma system.

by the floating potentials when the probe current is zero. The subscripts + and − are added when necessary to identify the probes on the $+y$ or $-y$ axes, respectively. The sheath resistances $R_s = \partial V_s / \partial i$ are given in terms of plasma parameters by

$$R_s = [U_e/(I_i + I_p)] \quad V \leqslant 0 \tag{5a}$$

$$R_s = [U_p/(I_e - I_i)] \quad V \geqslant 0 \tag{5b}$$

The voltage sources $E_y\,(l/2)$ and $E_y\,(-l/2)$ represent the plasma potential at the center of the two electrodes. As long as the sheath thickness is small compared to the antenna length, the effective length, l, of the antenna will be equal to the distance between the centers of the electrodes. R_B represents the input resistance of the differential amplifier, which is the same for each branch, $R_{B+} = R_{B-}$. We shall present the data in terms of 'measured' electric field E_M, defined as the measured probe potential difference, ΔV_M, divided by l. From the circuit diagram in Figure 3 it can readily be shown that the measured electric field E_M is given by

$$\begin{aligned} E_M &= E_1 + E_2 \\ E_1 &= \frac{E_y}{2}\left[\left(1 + \frac{R_{s-}}{R_{B-}}\right)^{-1} + \left(1 + \frac{R_{s+}}{R_{B+}}\right)^{-1}\right] \\ E_2 &= \left[\frac{V_-}{l}\left(1 + \frac{R_{s-}}{R_{B-}}\right)^{-1} - \frac{V_+}{l}\left(1 + \frac{R_{s+}}{R_{B+}}\right)^{-1}\right]. \end{aligned} \tag{6}$$

Ideally, the voltage drops across the sheaths of the two electrodes are identical,

$V_{s+} = V_{s-}$, and the sheath resistances are small compared to the differential amplifier input impedances, $R_s \ll R_B$. It follows from Equation (6) that in this case $E_M = E_y$ and the measured electric field is equal to the component of the electric field in the plasma parallel to the antenna axis.

4. Operation of the Injun-5 Electric Field Experiment

A. A MODEL FOR THE PROBE OPERATION

Numerical calculations of the operation of the Injun-5 double-probe system have been performed for the theoretical model just presented to evaluate various sources of error in the electric field determination and to compare the model with the observed operation in flight. The principal parameters which control the operation of the probe system are the electron density, n, the electron temperature, T_e, and the electric field component, E_y. Since the Injun-5 orbit includes altitudes from 677 to 2528 km, the electron number density may vary by several orders of magnitude. The electron densities, as measured by the AFCRL experiment on Injun 5, are commonly in the range 10^4 to 10^5 electrons cm^{-3}, but may be higher at perigee near the equator and occasionally as low as 10^3 electrons cm^{-3} at apogee over the polar caps (R. Sagalyn, private communication, 1970). In the numerical model we shall let n be an independent variable. The electron temperature T_e is less well known. The preliminary results of Sagalyn's experiment (private communication, 1970) on Injun 5 indicate a typical electron temperature of 2500 K, with temperatures sometimes higher than 10000 K and frequently about 5000 K at altitudes above 1500 km over the polar caps (at solar maximum). In the model we assume $T_e = 2500$ K, or else vary T_e independently. The calculation is insensitive to the ion temperature since the ion ram current, I_i, is caused primarily by the motion of the probe through the plasma.

The photo-electron current may differ for the two spheres at a given time due to either unequal shadowing or differences in the surface properties of the two spheres. Assuming that the latter effect is constant in time and independent of orientation, shadowing may be exploited to find approximate values for the photo-electron current, I_p, for each sphere. A study of 86 occasions when the spacecraft body shadowed one of the electric antenna spheres yields $I_{p+} = 3 \pm 1$ μA and $I_{p-} = 2 \pm 1$ μA (see Cauffman, 1971), for an average photo-electron yield of 8×10^{-5} A m^{-2}, in good agreement with expectations (see Fahleson, 1967). The difference $I_{p+} - I_{p-}$ can also be checked by examining transitions from the umbra region into sunlight (excluding situations with shadowing). A study of 26 such transitions implies that $I_{p+} - I_{p-} = 1.5 \pm 0.5$ μA. The asymmetry presumably arises from surface contamination of the spheres, perhaps during launch. Table III summarizes the values of parameters employed in the numerical model.

Figures 4 through 7 show results calculated using the probe system model. Figure 4 shows values for the floating potential, V, of a sphere as a function of electron number density, n, for a range of electron temperature values. These curves were calculated using Equations (4a, b). The potentials are typically a fraction of a volt negative.

For the values of T_i and T_e used in the calculation, the inequality ion velocity < satellite velocity ≪ electron velocity is also satisfied. Typical sheath thicknesses encountered in the Injun-5 orbit are less than the probe radius so that the effective length of the antenna, l, is to a good approximation equal to the distance between the centers of

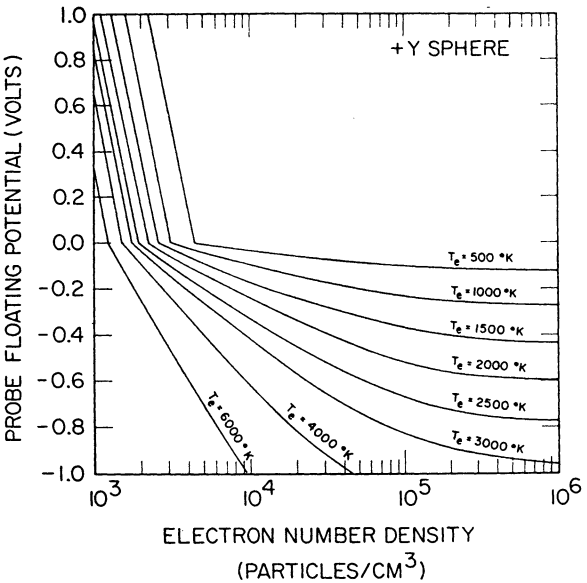

Fig. 4. Theoretical curves of probe floating potential as a function of electron number density and temperature.

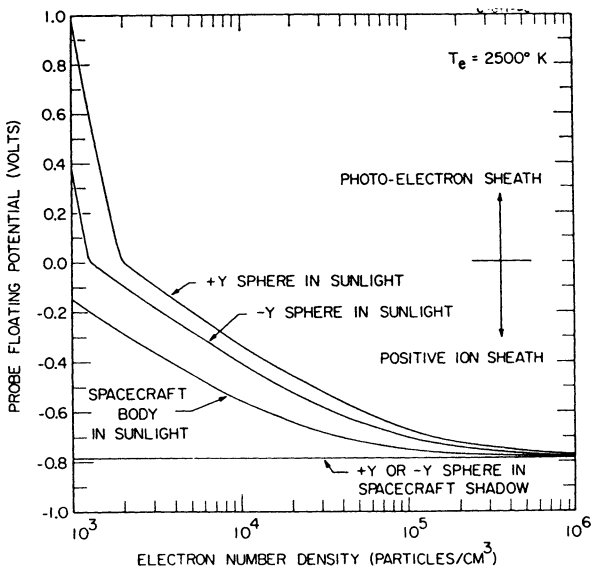

Fig. 5. Theoretical floating potential values of the electric antenna spheres and spacecraft body in sunlight and darkness.

the spheres. In Figure 5 the floating potential is shown for the two spheres and the spacecraft body. The difference in the floating potential for the $+y$ and $-y$ sphere is due to the previously mentioned difference in the photo-electron current for the two spheres. Figure 6 shows that in sunlight there is also a corresponding asymmetry in the sheath resistances of the two spheres.

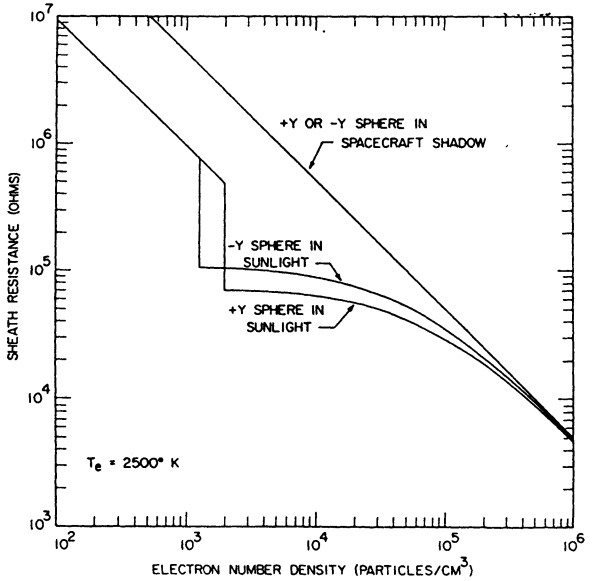

Fig. 6. Sheath resistances $\partial V/\partial i$ corresponding to the potentials shown in Figure 5.

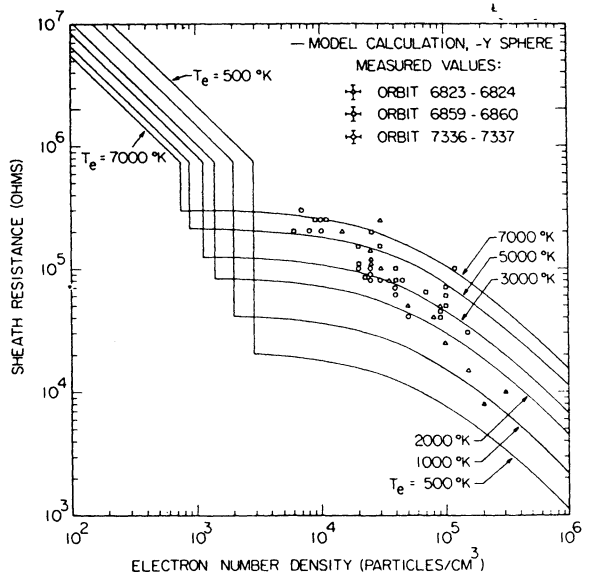

Fig. 7. Comparison of measured and calculated values of the probe-sheath resistance.

An independent test which may be applied to determine the quantitative correctness of the model is to compare predicted and measured values of the sheath impedance. The impedance measured by Injun 5 is found to be almost entirely resistive at 30 Hz and is attributed to the resistance of the plasma sheath around each probe (cf. Gurnett *et al.*, 1969). The points plotted in Figure 7 correspond to sheath resistances measured at various points around the Injun-5 orbit and the corresponding electron number densities measured simultaneously with the AFCRL experiment on Injun-5. Because T_e varies strongly with altitude, latitude, and local time, it is not expected that the measured points $R_s(n)$ will fall on any one calculated curve $R_s(n, T_e)$. In general the highest T_e will occur at high altitudes where n is low, and conversely. An examination of the measured vs. computed values in Figure 7 verifies that this occurs. Furthermore, the values of R_s observed fall on the theoretical curves corresponding to reasonable values of T_e. These facts suggest that there is good quantitative correspondence between the model predictions and actual probe behavior.

B. ERRORS

Because variations in measured electric fields not otherwise explained will be attributed to magnetospheric phenomena, considerable detail is justified in discussing errors. In this section we describe and explain the features of the data taken with the Injun-5 electric field experiment believed to be related to instrumental effects. Several of these features are shown in Figures 8 and 9. Each figure displays the electric field, the electric antenna impedance, and the electron number density measured during one orbit of the spacecraft.

The dashed lines in Figures 8 and 9 represent the magnitude of the $\mathbf{V}_s \times \mathbf{B}$ electric

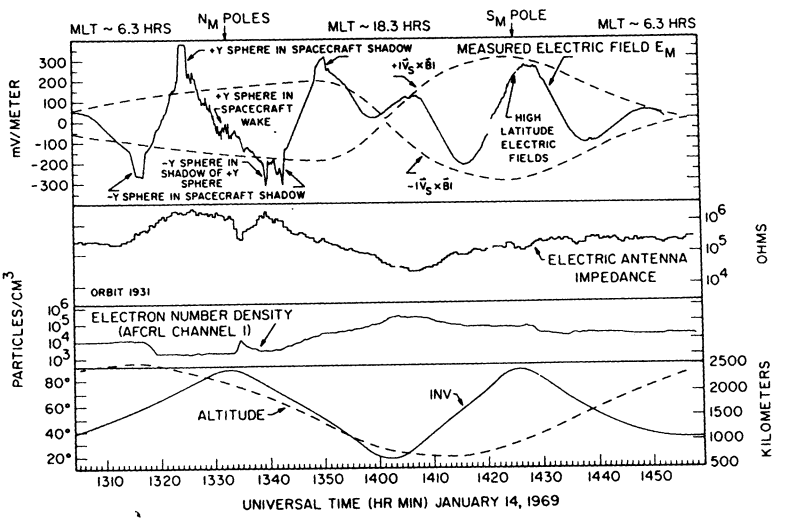

Fig. 8. Measured electric field, electric antenna impedance, and electron number density for a complete orbit of Injun 5 in the dawn-dusk plane.

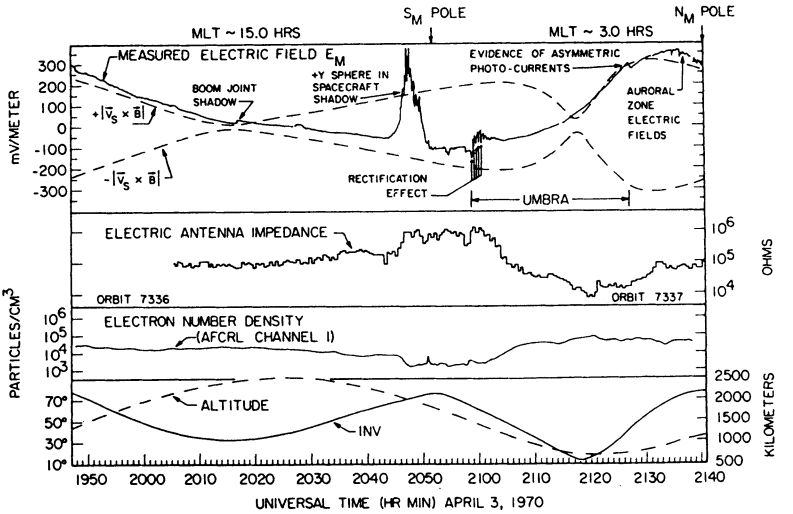

Fig. 9. Measured electric field, electric antenna impedance, and electron number density for a complete orbit of Injun 5 in the noon-midnight plane.

field in the reference frame of the satellite. $\mathbf{V}_s$ is the satellite velocity calculated from the Injun-5 orbit in a corotating coordinate system, and $\mathbf{B}$ is the geomagnetic field at the spacecraft position computed using the 1965 Cain *et al.* (1967) expansion for the geomagnetic field. Neglecting wake and shadow effects, the measured electric field E_M in Figure 8 has a sinusoidal shape modulated by the $\pm|\mathbf{V}_s \times \mathbf{B}|$ envelope. This sinusoidal shape is due to the satellite spin about the geomagnetic field with a period of about 20 min. When the $+y$ axis of the spacecraft is aligned parallel to $\mathbf{V}_s \times \mathbf{B}$, the measured electric field, E_M, is at a maximum. In Figure 9 the spacecraft is rotating very slowly, only a small fraction of a revolution per orbit. In the Northern Hemisphere the y axis of the satellite is nearly aligned with $\mathbf{V}_s \times \mathbf{B}$, so $E_y \cong +|\mathbf{V}_s \times \mathbf{B}|$. Since the direction of $\mathbf{V}_s \times \mathbf{B}$ reverses at the magnetic equator, $E_y \cong -|\mathbf{V}_s \times \mathbf{B}|$ in the southern hemisphere. During Injun-5's lifetime the spin rate has increased and decreased several times. Both senses of spin about the geomagnetic field directions have occurred.

1. *Shadow Effects*

The large perturbations in Figures 8 and 9 labeled 'spacecraft shadows' occur when the photo-electron current to one of the spheres changes as the sphere enters the sunlight shadow of the spacecraft body. Figure 10 shows the calculated magnitudes of the quantites $E_1(E_y)$ and $E_2(V)$ introduced in Equation (6) for darkness, sunlight, and shadow conditions. If $R_s \ll R_B$, $E_1 = E_y$ represents the real electric field y component measurable in the satellite reference frame. Under ideal conditions of sphere symmetry in every respect, $E_2 = 0$.

It is evident from Figure 10 that the behavior of E_2 when either sphere is shadowed

is consistent with the observed directions, positive (negative) for shadows on the $+y$ $(-y)$ sphere, and magnitudes, larger near the poles where n is low, of shadow perturbations as illustrated in Figures 8 and 9. Increases in the impedance often accompany the occurrence of shadows on the spheres, as predicted in Figure 6. Since the electric field antenna booms and boom joints can shadow as much as 20% of the surface of a probe, the effects of boom shadows are proportionately smaller than

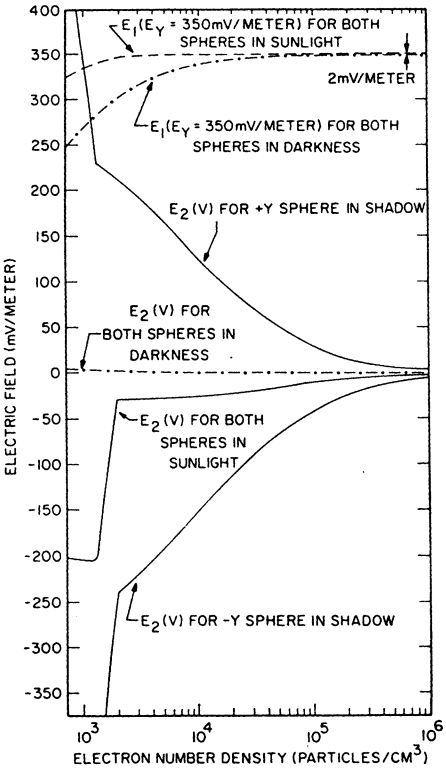

Fig. 10. Values of the terms E_1 and E_2 (see Equation (6)) calculated for sunlight and shadow conditions for Injun 5.

those indicated for total sphere shadowing. Maximum boom shadowing errors are therefore expected to be about 40 mV m^{-1}.

For orbits in the dawn-dusk plane, such as the orbit shown in Figure 8, shadows caused by the supporting booms (cf. Figure 1) are unequal for the two spheres at orientations corresponding to peaks and valleys in the $\mathbf{V}_s \times \mathbf{B}$ electric field. As illustrated in Figure 8, this asymmetrical boom shadowing effect adds to peaks in the measured $\mathbf{V}_s \times \mathbf{B}$ field in one hemisphere and subtracts from peaks in the measured $\mathbf{V}_s \times \mathbf{B}$ field in the other hemisphere, because $\mathbf{V}_s \times \mathbf{B}$ reverses direction at the equator. For noon-midnight orbits, boom shadowing is symmetrical on the two spheres at

peaks and valleys in the measured $\mathbf{V}_s \times \mathbf{B}$ field (cf. Figure 7 of Cauffman, 1971). In this case E_M equals $\pm \mathbf{V}_s \times \mathbf{B}$ at peaks and valleys to within 10 mV m^{-1}.

2. *Earth Shadow Effects*

Figure 9 illustrates two separate effects which occur at low electron densities when the spacecraft is in darkness within the Earth's umbra: (1) a change in the electric field toward zero (which in Figure 9 is a positive change in E_M), and (2) several negative spikes in the electric field measurement. As discussed below, the change in the electric field toward zero within the umbra is believed to be caused by the increase in the sheath resistance when the photo-electron current goes to zero within the Earth's shadow. The negative spikes correspond exactly to the times that the impedance measurement is made, and may be explained as a rectification of the impedance measurement driving current due to asymmetries in the electric antenna system. This effect is discussed in more detail by Cauffman (1971).

The probe behavior in the Earth's shadow can be determined from the model calculations shown in Figure 10. The discrepancy between E_1 in sunlight and E_y, as shown in Figure 10, is caused by the finite amplifier resistance in the factor $(1 + R_s/R_B)^{-1}$ of Equation (6). In the Earth's shadow when the photo-electron current, I_p, disappears from Equations (5a, b), the sheath resistance increases as the electron density, and correspondingly the ion ram current I_i, decreases. We attribute the change towards zero electric field, which appears in Figure 9 (ignoring the spikes) as the satellite enters the Earth's shadow, to this cause. A corresponding increase in the measured sheath resistance is also observed at this time. As the electron density increases towards lower latitudes the effect disappears. For the example in Figure 9 the magnitude of the change is about 50 mV m^{-1}, while the AFCRL electron density experiment indicates an electron density of about 2×10^3 electrons cm^{-3}, in good agreement with the magnitude predicted by the model.

Figure 10 predicts that in darkness the error term E_2 is indeed nearly zero as ideally expected. However, in sunlight, the sphere floating potentials are different (see Figure 5) due to the unequal photo-electron emission for the two spheres. Excluding values when the electron densities are below 2×10^3 electrons cm^{-3}, Figure 10 shows that E_2 may be as large as -30 mV m^{-1} in sunlight. This is in exact agreement with the magnitude and direction of the jump in E_M observed when the spacecraft goes from the Earth's umbra into sunlight at 2127 UT in Figure 9. The spheres were not shadowed at this time by the spacecraft booms or body. E_2 for both spheres in sunlight may vary by up to 20 mV m^{-1} as n varies slowly with altitude and latitude around the Injun-5 orbit. Like boom shadowing, the error due to the unequal photo-electron emission for the two spheres contributes to the difference between E_M and $\hat{y} \cdot \mathbf{V}_s \times \mathbf{B}$, and is virtually impossible to calculate. The method for eliminating these effects will be discussed in Section C. The combination of an error of up to 20 mV m^{-1} due to the unequal photo-electron emission for the two spheres and an error of up to 40 mV m^{-1} due to boom shadowing gives a maximum error between the measured $\mathbf{V}_s \times \mathbf{B}$ field and the computed $\mathbf{V}_s \times \mathbf{B}$ field. This maximum error is in good agreement

with the maximum discrepancies observed between the $|\mathbf{V}_s \times \mathbf{B}|$ envelope and the maxima and minima of the sinusoidal $\mathbf{V}_s \times \mathbf{B}$ field observed in Figure 8 and in other similar cases.

In Figure 9 the satellite crosses the Earth's umbra with the electric antenna axis nearly parallel to the direction of $\mathbf{V}_s \times \mathbf{B}$ in the northern hemisphere. The measured electric field fails to go through zero at the midnight equator where $\mathbf{V}_s \times \mathbf{B}$ changes sign even though both the error due to unequal photo-electron emission and the error due to boom shadowing are zero because the spacecraft is in darkness. This error corresponds to a 0.14 V difference in the contact potential for the two spheres. The difference in the contact potentials does not affect the results of the electric field experiment other than shifting its zero point. In sunlight the contact potential difference is almost completely cancelled by the error due to the unequal photo-electron emission of the two spheres. As shown in Figure 9, at the sunlit equator the electric field measurement misses zero by just 20 mV m^{-1}. (Prior to the boom joint shadow indicated at 2018 UT, neither sphere was shadowed.) The difference between the amounts by which E_M exceeds zero at the two equators is 30 mV m^{-1}, which corresponds exactly to the 30 mV m^{-1} jump attributed to the unequal photo-electron current evident at 2127 UT in Figure 9. Furthermore, the sheath impedance at the sunlit equator is $R_s \cong 8 \times 10^4\ \Omega$. In the linear approximation, therefore, the difference in the photo-electron current for the two spheres should be

$$\Delta I_p \cong \frac{l|\Delta E|}{R_s} = 1.1\ \mu\text{A}.$$

This value is in agreement with the results of the shadow study previously mentioned. The consistency evident in the observations of contact potentials, umbra transition discontinuities, shadowing magnitudes, and sheath impedances promotes confidence in the numerical model, which correctly reproduces their interrelationship.

3. *Wake Effects*

The satellite velocity $\mathbf{V}_s$ exceeds the thermal ion velocity at Injun-5 altitudes. As a result, ions are swept away by the moving spacecraft and a rarefied wake region exists behind the satellite. Because approximate charge neutrality must be maintained, electrons cannot enter the wake until the heavier, slower ions do. Hence the wake region is rarefied and has a slightly negative potential. The large negative perturbation in Figure 8 labeled 'spacecraft wake' occurs when the $+y$ sphere enters the satellite's velocity wake. Figure 11 shows the correlation between wake effects and the angle between the $+y$ sphere and $-\mathbf{V}_s$, on three successive passes over the north polar cap. The $\mathbf{V}_s \times \mathbf{B}$ field has been subtracted from the electric field data shown. Tables IV and V give the results of a study of 451 occasions when one sphere came within 30° of the $-\mathbf{V}_s$ vector. Any clearly distinguishable electric field perturbation which correlated with the minimum angle to $-\mathbf{V}_s$ was classified as a wake effect in this study, so some naturally occurring electric field events may be included by chance.

The model of probe behavior predicts that when the electron number density in the

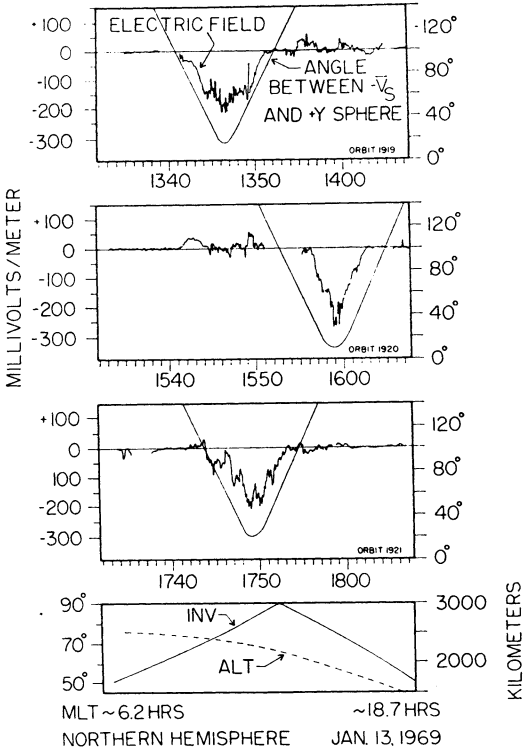

Fig. 11. Spacecraft wake effects observed on 3 successive high-altitude passes with Injun 5.

probe vicinity drops below $\sim 2 \times 10^3$ electrons cm^{-3}, the probe floating potential becomes positive with respect to the plasma potential and a photo-electron sheath is formed (see Figure 5). Equation (6) indicates that if the $+y$ $(-y)$ sphere potential increases, then the measured electric field E_M will decrease (increase). This dependence is in agreement with the observations of wake effects reported in Table V. Furthermore, as shown by Figure 5, a photo-sheath forms around the $+y$ sphere at higher

TABLE IV

Occurrence of wake effects

	Impedance (Ω)		
Altitude (km)	10^4–9×10^5	10^5–9×10^6	$>10^6$
>2500	(0)	5% (22)	55% (11)
2000–2400	(0)	11% (27)	58% (52)
1500–1900	(0)	15% (106)	76% (21)
1000–1400	0% (2)	4% (119)	100% (1)
500– 900	3% (31)	0% (53)	(0)
All altitudes	3% (33)	8% (327)	62% (85)

Numbers in parentheses indicate number of samples.
Total number of samples (probe within $\pm 30°$ of $-V_S$): 445.

TABLE V

Probe potential in the spacecraft wake

	Sphere 1		Sphere 2	
+potential[a]	95%	(54)	88%	(22)
−potential[a]	5%	(3)	12%	(3)
both potentials[b]	26%	(57)	11%	(25)
total samples		(222)		(229)

Numbers in parentheses indicate number of samples (probe within $\pm 30°$ of $-V_s$).

[a] Percent of samples for this sphere exhibiting wake effects.

[b] Percent of total samples for this sphere.

electron densities than for the $-y$ sphere. It is therefore expected that wake effects should be observed more frequently when the $+y$ sphere is in the wake region than when the $-y$ sphere is in the wake. This prediction, also, agrees with observations (see Table V). Figures 6 and 7 show that the impedance should rise dramatically to $\gtrsim 10^6\ \Omega$, when a photo-sheath forms. Table IV verifies that high measured impedances accompany wake effects (e.g. see Figure 8). During the orbit shown in Figure 8 the electric antenna spheres entered the wake region seven times, in both hemispheres. Nevertheless only one wake effect occurred, and that event occurred when the $+y$ sphere was in the wake, at high altitude, high impedance, and low electron number density. Quantitative comparisons of theory and observation are not possible because densities and temperatures in the wake region are unknown. However, on the basis of the excellent qualitative agreement of these predictions of wake effects with observations, we conclude that wake effects are in fact caused when one probe develops a photo-electron sheath in the rarefied region behind the moving spacecraft.

4. *Variations and Gradients in Plasma Parameters*

The effect of variations in the electron density and temperature may be investigated by taking partial derivatives of Equation (6) with respect to these quantities. The effect of gradients may be found by evaluating Equation (6) using different parameters at the

TABLE VI

DC electric field phenomena observed at the auroral zone

	Number of cases	Percent occurrence
Single convection zones	66	23
Reversals (two oppositely-directed convection zones)	102	36
Noise (multiple convection zones)	57	20
Noise extending across the polar cap	25	9
Quiet ($\|E_c\| < 10$ mV m^{-1})	36	13
	Total 286	

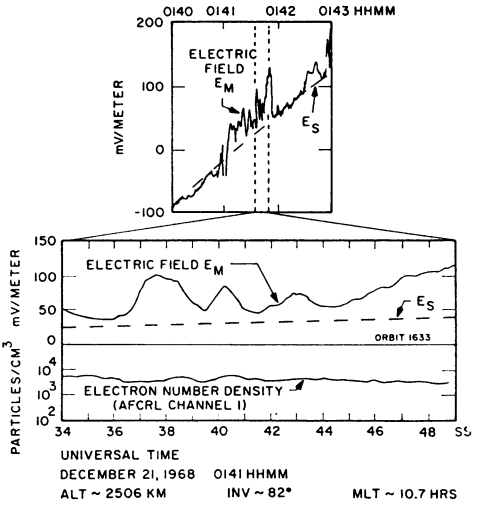

Fig. 12. Comparison of Injun-5 DC electric field and electron number density fluctuations taken at apogee.

two spheres. The results of such a calculation using the numerical model with large gradients and variations indicate that for electron densities $\geqslant 2 \times 10^3$ electrons cm^{-3}, errors of less than 10 mV m^{-1} will be produced (Cauffman, 1971).

However, we need not rely on the theoretical calculation. Experimental evidence can be given that electron density and temperature gradients have negligible effects on the electric field measurement. Although electron number densities or temperatures measured by the AFCRL experiment on Injun 5 frequently exhibit fluctuations in the same intervals when electric field noise is observed, the AFCRL data and the electric field variations do not correlate on a one-to-one basis. Figures 12 and 13 show 'worst-

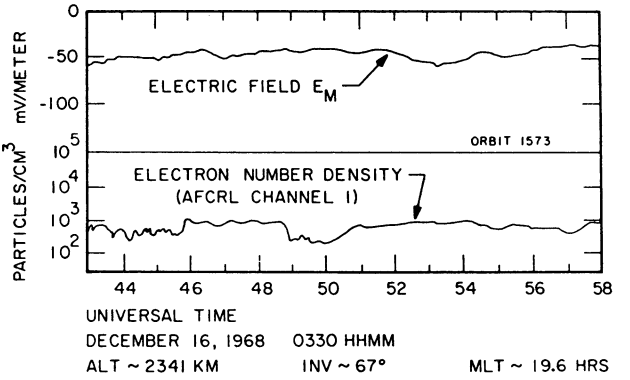

Fig. 13. Comparison of Injun-5 DC electric field and electron number density fluctuations taken at apogee.

case' examples of both electric field and number density fluctuations. These data were taken in the high data rate mode during apogee polar passes in the northern hemisphere in winter. The AFCRL experiment in fact measures a quantity proportional to $n\sqrt{(T_e)}$. (A constant electron temperature of 2500 K has been assumed in calibrating the scale.) It is evident that the fluctuations shown as due to number density variations could alternatively be due to electron temperature variations. The lack of correlation of the AFCRL and electric field data may therefore be taken as an indication that neither n nor T_e variations which exist directly affect the electric field measurement. In Figure 12 large ($\geqslant 50$ mV m^{-1}) electric field fluctuations occur but only small variations in n (or T_e) occur. Figure 13 shows electron density (or temperature) fluctuations of $\geqslant 100\%$, but these fluctuations show no relationship to the variations in electric field observed.

5. *Energetic Charged Particles*

Over the auroral zones Injun 5 encounters intense fluxes of energetic charged particles. In order to affect the operation of the electric field experiment the current contribution from energetic charged particles must be different for each sphere. Because the gyroradius of a 50 eV electron is about one meter or greater at Injun-5 altitudes, no significant gradients are expected in the 2.85 m between spheres. An upper limit for >50 eV electron flux encountered in the Injun-5 orbit is $J_e \cong 5 \times 10^8$ particles cm^{-2} s. (L. A. Frank, private communication, 1971). This flux corresponds to a density of

$$n_e(>50 \text{ eV}) \frac{J_e}{|V_e|} \cong 1 \text{ electron cm}^{-3}$$

assuming 50 eV electrons. As this density is about 0.1% of the lowest thermal electron densities encountered in the Injun-5 orbit, errors due to energetic particle fluxes are considered to be negligible.

C. DATA ANALYSIS

1. *Magnetospheric Electric Field Determination*

In order to determine naturally occurring electric fields it is necessary to subtract the $\mathbf{V}_s \times \mathbf{B}$ electric field and other instrumental effects from the measured electric field. Spacecraft shadows and 'steps' at the edge of the umbra can easily be identified from spacecraft attitude and orbital parameters. For Injun-5 data, all remaining errors are found to be less than 10 mV m^{-1} except at electron densities predicted by the model to be less than about 2×10^3 electrons cm^{-3}, below which photo-sheaths begin to form around the spheres. A criterion for the possibility of large errors has been developed based on observations, rather than on the model. The study of 451 spacecraft wake predictions discussed in Section B3 and summarized in Tables IV and V shows that wake effects are indicated by the occurrence of impedances greater than 10^6 Ω. The impedance measurement thus provides a rigorous observational test of the quality of the electric field data. If the impedance is greater than 10^6 Ω, the electric field

measurements are discarded. For impedances less than 10^6 Ω, a limit on the contributions due to all errors except the various manifestations of shadowing and slow changes in plasma parameters around the Injun-5 orbit may be set at ± 10 mV m^{-1}. The only problem which remains is to correct for the smooth long term variations ($\lesssim 50$ mV m^{-1}) caused by boom shadowing and the unequal photo-electron emission from the two spheres. Because of uncertainties in the various plasma parameters involved, these errors cannot be calculated with sufficient accuracy to be useful.

The procedure which has been adopted for subtracting the $\mathbf{V}_s \times \mathbf{B}$ field and the boom shadowing error from Injun-5 data is the following: a smooth curve E_s is hand-drawn through the measured electric field subject to three requirements:

(1) It has a sine wave shape which is qualitatively the same as the computed component of $\mathbf{V}_s \times \mathbf{B}$ parallel to the antenna axis.

(2) The modulation amplitude and phase are adjusted to provide a good fit a low latitudes where no convection electric fields are expected.

(3) In cases of uncertainty the curve is drawn closer to the average measured field.

The residual electric field, $E_c = E_M - E_s$, attributed to magnetospheric electric fields, will in general *underestimate* the actual naturally occurring electric field. If natural electric fields occur which are small and uniform for times comparable to the rotation period of the spacecraft, they will unfortunately but unavoidably be subtracted out by this data reduction procedure and will not appear in E_c. The absolute values of E_s and E_c cannot usually be determined more accurately than about ± 30 mV m^{-1}. However, when the spacecraft is rotating slowly, boom shadowing is excluded for some orientations, and the magnitude of E_c can be determined to an accuracy of ± 10 mV m^{-1}. Also, fluctuations in the E_c electric field which occur with periods much less than the satellite spin period are considered significant if their magnitude exceeds 10 mV m^{-1}.

The left-hand side of Figure 14 illustrates the data reduction procedure used to determine the convection electric field, E_c, for a typical polar pass. E_s is the smooth curve drawn to best approximate the $\mathbf{V}_s \times \mathbf{B}$ field and the boom shadowing error. The residual electric field, $E_c = E_M - E_s$, has abrupt reversals of approximately ± 30 mV m^{-1} at 2225 and 2234 UT. The angles between the probes and the velocity vector, θ_s, verify that for these events neither probe was in a shadow. The angles between the probes and the velocity vector, θ_v, indicate that the $+y$ sphere was in the wake region at 2234 UT, but because the impedance is much less than 10^6 Ω, we know that no photo-sheaths formed, so the event at this time could not be due to a wake effect. Hence, these electric field reversals are assumed to be due to naturally occurring magnetospheric electric fields.

2. *Convection Velocity Determination*

Axford (1969) has explained that at Injun-5 altitudes the conductivities are such that the electric field is related to the convection velocity $\mathbf{V}_c$ of the plasma by the equation

$$\mathbf{V}_c = \mathbf{E}_c \times \mathbf{B}/B^2 . \tag{7}$$

The convection velocity components associated with the electric fields shown in the left-hand side of Figure 14 are illustrated on a magnetic local time/invariant latitude polar diagram in the right-hand side of Figure 14. Each arrow represents the *measured component* of the convection velocity computed using Equation (7). The length of the arrow is proportional to the magnitude of V_c and the direction of the convection velocity during the interval. It must be emphasized that

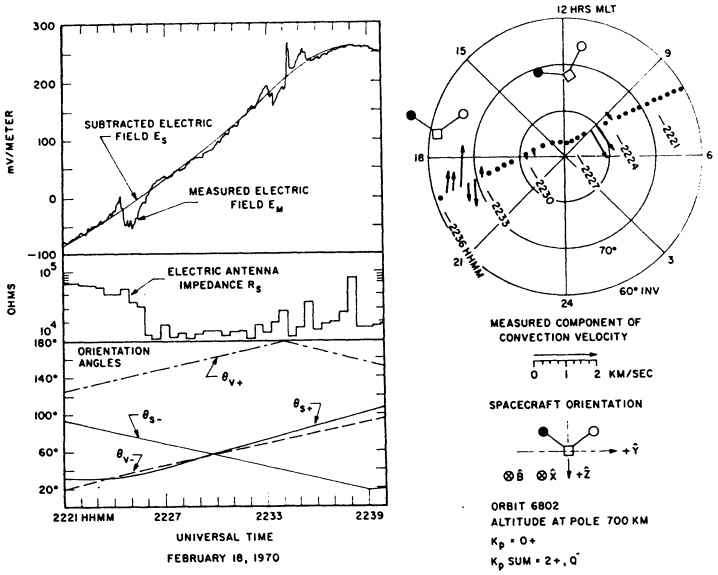

Fig. 14. Examples of a polar pass illustrating the Injun 5 data reduction procedure. *Left:* The convection electric field is assumed to be given by $E_c = E_M - E_s$. *Right:* Arrows representing the magnitude and direction of the component of convection velocity calculated from $V_c = (E_c \times B)/B^2$. *The arrow does not represent the true convection velocity, but only the one component measured.*

the arrow represents only the component of the convection velocity detected; it does not represent the vector direction of the convection velocity since only one component is measured. Because of the orientation of the spacecraft during the events shown in Figure 14, the north–south component of the convection velocity cannot be determined.

Since the satellite is rotating very slowly and boom shadowing cannot occur for the orientations shown in Figure 14, the convection velocity component can be determined very accurately for this example. In general the magnitudes of convection velocity variations determined for intervals much smaller than the satellite rotation period are believed to be uncertain by about 0.25 km s^{-1} and, as in the case of E_c, represent a lower limit. However, uniform convection velocities for times comparable to the Injun-5 spin period are not expected to be detectable if the convection velocity is less than about 0.75 km s^{-1} because slowly-varying electric fields are eliminated in the data reduction procedure.

5. Observations

A. OBSERVATIONS WITH INJUN 5

1. *General Observations*

Significant DC electric fields not attributable to any known instrumental effect are observed at middle and high latitudes on nearly every orbit of the Injun-5 satellite. At the plasmapause/light ion trough boundary small (10–20 mV m^{-1}) electric field perturbations are sometimes observed, generally corresponding to westward convection outside the plasmasphere. At high altitudes, above about 1500 km, over the auroral zone/polar cap, regions of irregular electric field fluctuations called 'noise' with time scales generally less than 60 seconds are consistently detected (cf. Figure 12). The general characteristics of both electric field noise and plasmapause effects are discussed by Cauffman and Gurnett (1971b).

2. *Observations of Electric Field Reversals*

a. *General Characteristics.* Frequently at the auroral zone electric field perturbations are observed which take the form of reversals in the electric field direction. The occurrence of such reversals does not depend on sheath impedance or spacecraft orientation. An example of an electric field reversal has been shown in the left-hand side of Figure 14 at 2125 UT. In the right-hand side of Figure 14 the same reversal is interpreted in terms of an $\mathbf{E} \times \mathbf{B}/\mathbf{B}^2$ convection velocity. On both sides of the reversal are 'zones' of oppositely-directed thermal plasma convection. Table VI gives the occurrence statistics, for 286 auroral zone crossings, of 'noise' (more than 2 zones; e.g. see Figure 14 at ~2234 UT), reversals (2 zones), single zones, and quiet crossings ($|\mathbf{E}_c| < 10$ mV m^{-1}). Reversals have been chosen for a detailed study because they occur most frequently, they evidently identify a boundary which is of fundamental significance with regard to magnetospheric structure, and they are the most reliably measured electric field phenomenon. The signature of a reversal cannot arise due to a spurious shadow, and the peak-to-peak magnitude is unaffected by the data reduction procedure. Cauffman (1971) provides further details of the study reported in this section. Supplementary examples of Injun data may be found also in Cauffman and Gurnett (1971b).

Figure 15 shows a series of successive orbits over the Northern Hemisphere which illustrates the persistent occurrence of electric field reversals at latitudes of 70° to 80° INV. Usually the largest convection velocities are observed near, within 5° to 10° INV, the electric field reversal location. At higher latitudes, in the polar cap region, the convection velocity is generally less than the ~0.75 km s^{-1} sensitivity limit imposed by the ±30 mV m^{-1} uncertainty in the convection electric field determination. Orbit 6909, in Figure 2, shows the occurrence of an essentially uniform anti-sunward flow with velocities greater than 1 km s^{-1} along the entire satellite trajectory over the polar region from 1724:00 to 1734:00 UT. Examples of relatively uniform transpolar convection, such as might be inferred from cases like orbit 6909, with convection

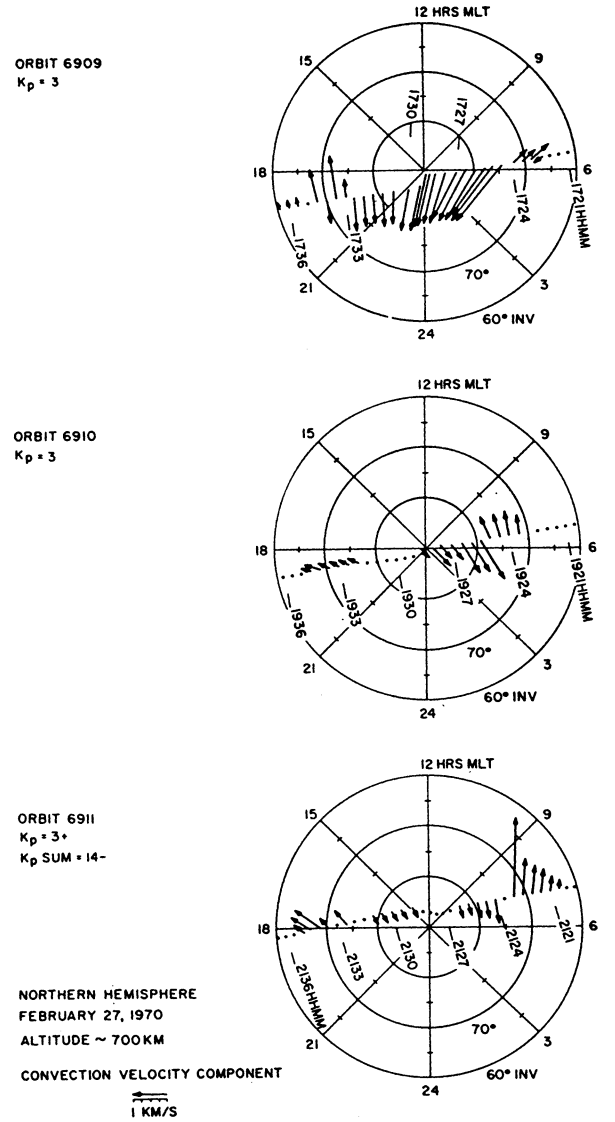

Fig. 15. Convection velocity reversals observed to occur on conjugate ends of the same geomagnetic field lines, one hour apart, with Injun 5.

velocities greater than 0.75 km s^{-1} are not commonly observed with Injun-5. Other orbits, such as shown in Figure 6 of Cauffman and Gurnett (1971a), have demonstrated that the electric field reversals occur at nearly conjugate locations in opposite hemispheres and that near the reversal location the convection velocity is generally east–west with only a small north–south component.

In Figure 16 six successive polar cap crossings in the noon-midnight plane are shown. The plasma convection detected at auroral latitudes is consistent with the interpreta-

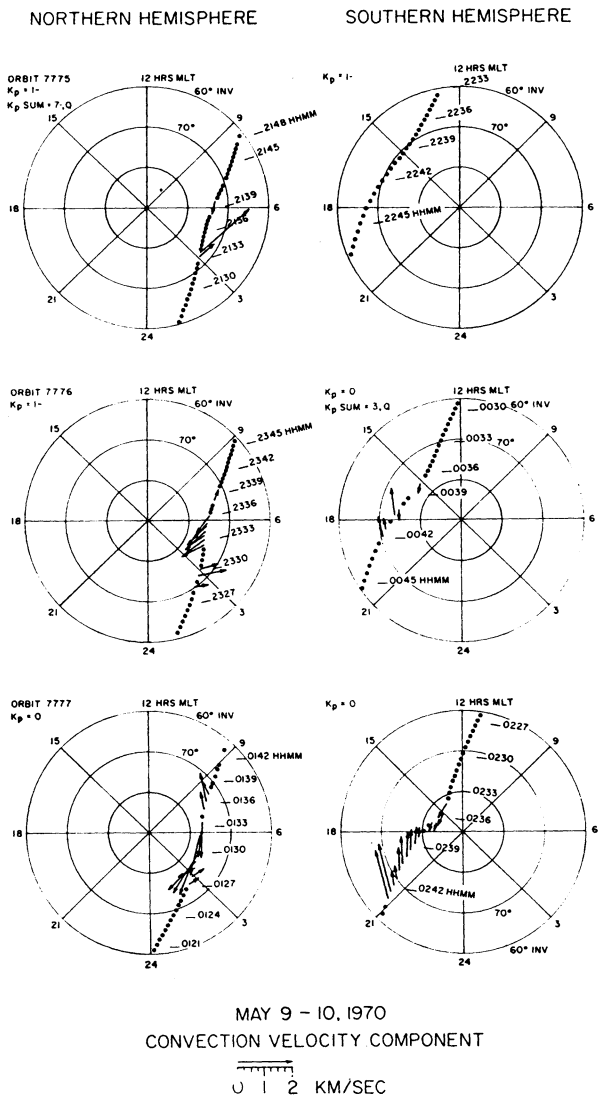

Fig. 16. Components of plasma convection measured with Injun 5 on six polar passes during a magnetically quiet period.

tion that the satellite path sliced through narrow longitudinal bands of convection which were directed sunward at latitudes below about 75° INV and anti-sunward at higher latitudes. The width of the convection zones observed appears greater before dawn and after dusk.

In the 2 h between satellite passes over a polar cap the magnitudes of the convection components often change significantly, the widths of the zones change, and the invariant latitude of the reversal shifts by several degrees. Thus the time scales of the

reversal phenomenon are shorter than the two hours between passes, although the overall pattern generally persists.

The peak magnitudes of convection velocities observed in individual zones average 1.5 km s^{-1} and include speeds greater than 5 km s^{-1}. The maximum magnitudes of convection observed do not vary systematically as a function of local time. In general the maximum convection velocities at latitudes above and below reversals are unequal.

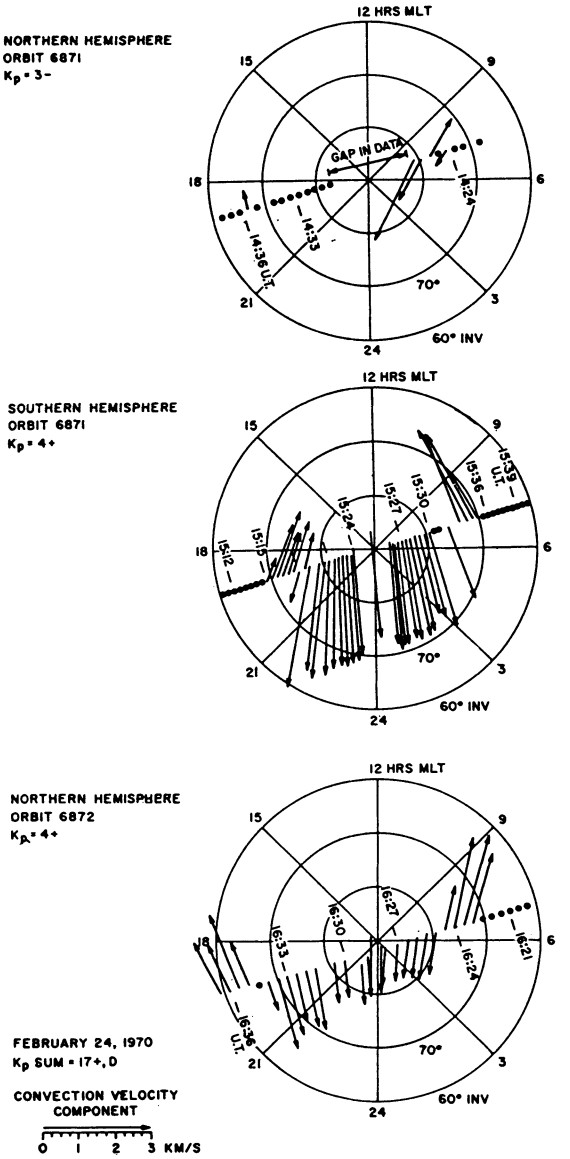

Fig. 17. Large-scale anti-sunward convection observed with Injun 5 over both poles during a magnetically disturbed period.

The average width of convection zones (excluding zones extending across the entire polar cap) is often widest just before dawn and just after dusk. The widths of the zones on each side of reversals are in general not equal.

For about 14% of reversals, the convection zone on the high latitude side of the reversal does extend across the polar cap. Figure 17 shows the largest example of this trans-polar convection encountered in the Injun-5 data. In most cases the magnitude of convection across the polar cap cannot be determined more accurately than ± 0.75 km s^{-1}.

In a few cases, however, due to slow spacecraft rotation or orientations precluding boom shadowing, the absolute magnitude of polar cap convection can be determined to be less than 0.25 km s^{-1}. Figures 18 and 19 show two of these cases. In these examples E_s can be drawn more accurately than ± 10 mV m^{-1}, so the convection velocity components determined are accurate to less than ± 0.25 km s^{-1}. For the cases shown in Figures 18 and 19 the V_c component measured is small (<0.25 km s^{-1}) over

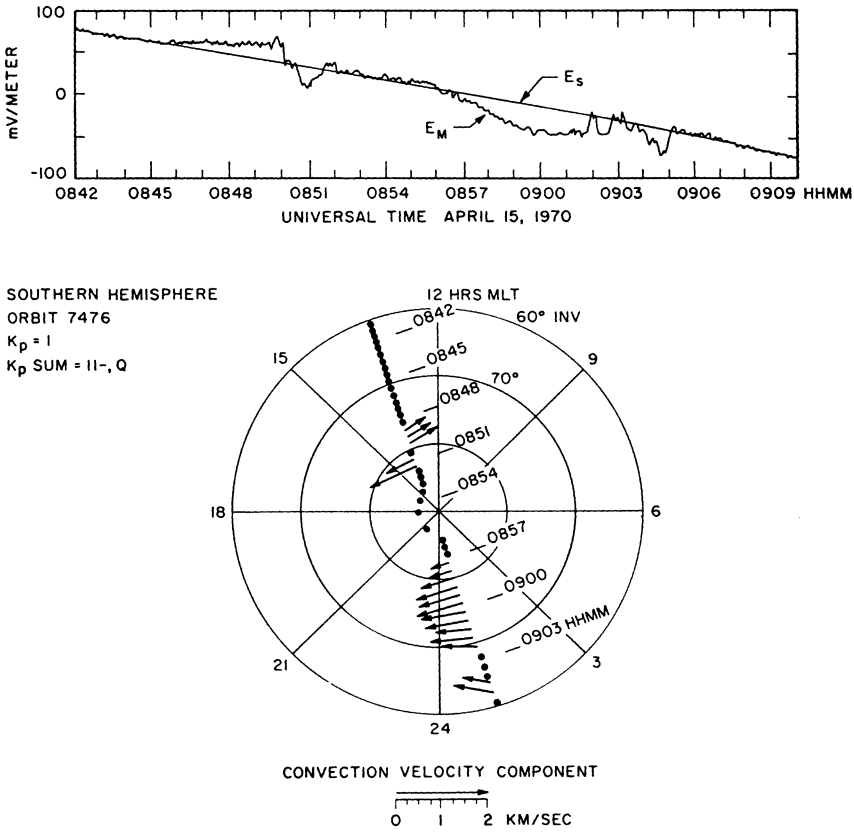

Fig. 18. DC electric fields and derived plasma convection velocity components observed when the Injun-5 satellite was slowly rotating. The accuracies of the measurements in these favorable circumstances are ± 10 mV m^{-1} for $E_c = E_M - E_s$ and ± 0.25 km s^{-1} for $V_c = E_c \times B/B^2$.

the center of the polar cap and the major convection occurs in zones at auroral zone latitudes separated (except near midnight) by electric field reversals.

A catalogue of 112 examples of electric field/convection velocity reversals has been compiled (Cauffman and Gurnett, 1971b). The points in Figure 20 show the locations of these reversals in invariant latitude and magnetic local time. The relative occurrence of reversals as a function of MLT is determined by the satellite orbit and data coverage.

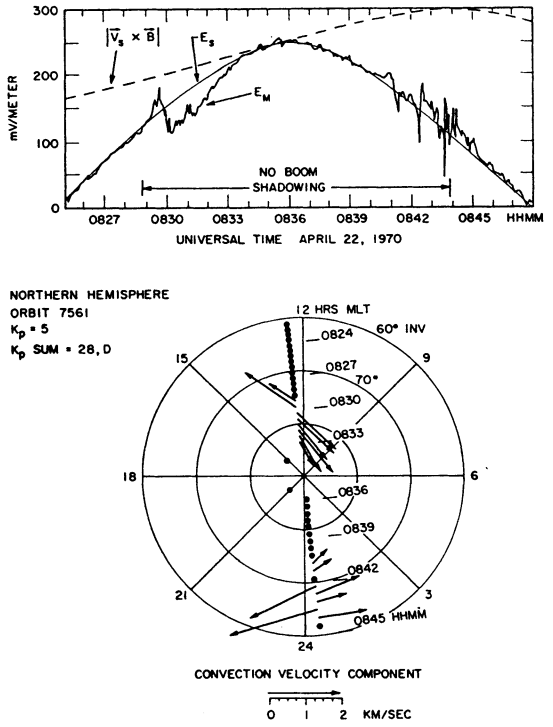

Fig. 19. DC electric fields and derived plasma convection velocity components observed when the Injun-5 satellite was slowly rotating. The accuracies of the measurements in these favorable circumstances are ± 10 mV m^{-1} for $E_c = E_M - E_s$ and ± 0.25 km s^{-1} for $V_c = E_c \times B/B^2$.

It is evident in the figure that reversals tend to occur at 75° to 80° INV near noon, at 60° to 75° INV near midnight, and at intermediate invariant latitudes near dawn and dusk. Individual exceptions occur. It is not known for certain whether the cluster of reversals observed between 80° and 85° INV at dawn and dusk is a result of the greater amount of data which is available in those sections or represents an increased probability of observing reversals in these regions.

b. *Convection Directions.* The convection shown in Figures 14 through 19 illustrates the persistent occurrence of reversals in the east–west direction of the convection in the auroral zone. In most of these cases the primary convection pattern is limited to a region several degrees in latitude on either side of the reversal with sunward convec-

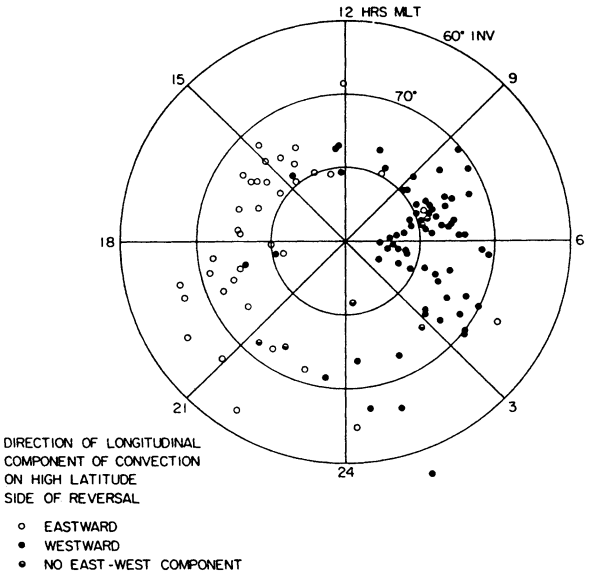

Fig. 20. Locations in invariant latitude and magnetic local time of 112 reversals observed with Injun 5. The points are coded to show whether the measured component of convection velocity on the high latitude side of each reversal had eastward or westward components.

tion generally observed on the low latitude side of the reversal and anti-sunward convection on the high latitude side of the reversal. Broad convection zones with velocities greater than 0.75 km s^{-1} over the polar region, such as those evident in Figure 17, are less common.

Although only one component of convection velocity is measured, it is possible to deduce the general direction of the plasma flow from large numbers of observations. The points in Figure 20 are coded to show which of the 112 reversals studied had eastward flow components measured on the high latitude sides of the reversals, and which had westward components. (The directions of flow components measured on the low latitude sides of the reversals are opposite to those indicated, because the spacecraft does not rotate significantly in the time required to detect a reversal.) It is clear from the figure that nearly all reversals which occur at MLT between 0 and 12 h have westward convection components measured on the high latitude sides of the reversals. Similarly, between 12 and 24 h MLT, most reversals possess eastward flow components on their high latitude sides. When the 112 reversals are analyzed with respect to poleward vs. equatorward measured convection components, the distribution appears to be random. Randomness would be expected, due to arbitrary satellite orientation, if the true convection direction were generally east or west. The contention that the true convection direction is generally east or west is further supported by the fact that a large number of reversals (21) have no north–south component, while few (7) have no east–west component. We conclude, on the basis of these statistical results and on the basis of interpretation of individual cases such as that at 1643 UT in Figure 15,

that the true convection directions are primarily westward at local times less than about 12 h, and eastward at local times greater than 12 h, on the poleward sides of reversals, and opposite on the equatorward side.

In addition to the general convection directions described, the Injun-5 study of DC electric field reversals has provided evidence that

(1) convection velocities are ordinarily less than 0.75 km/sec over the polar cap region;

(2) convection zones tend to be the widest just before dawn and after dusk;

(3) even near noon, convection directions associated with reversals are generally east or west, not north or south;

(4) near midnight some north or south convection may occur;

(5) convection magnitudes are greatest near reversals; and

(6) convection magnitudes tend to be greater at night than in day local times.

These features represent a gross simplification of the actual convection, which is often chaotic or turbulent, and highly variable in time. Furthermore, in selecting reversals for study, constant fields of less than 30 mV m^{-1} have been neglected.

c. *Magnetic Activity Dependence.* In many cases large convection velocities occur when K_p is low, and conversely. The relative occurrence of reversals is only weakly a function of K_p (Cauffman, 1971). A detailed comparison of convection with substorm phenomena is required to determine better the relationship between the convection magnitudes and magnetic activity. It should be pointed out that the large-scale convection shown in Figure 17 occurred on a disturbed day when K_p was +4. Large disturbances in 7 north polar cap magnetograms occurred about an hour *after* this large trans-polar convection was first observed.

d. *Association with Energetic Charged Particles.* The association between electric field reversals and energetic charged particles has been investigated by Frank and Gurnett (1971). They have found that electric field reversals are coincident with the high latitude termination of measurable intensities of >45 keV energetic electrons, as shown in Figure 21. Also shown in this figure are the intensities of low energy protons and electrons measured by the LEPEDEA detector on Injun-5 (cf. Frank *et al.*, 1966). The peaks in the low energy electron intensities are an index to the location of inverted 'V' type precipitation events described by Frank and Ackerson (1970). As discussed by Frank and Gurnett (1971) inverted 'V' precipitation events of this type are observed near the electric field reversal location.

e. *Summary.* Electric field reversals are the most significant convection electric field effect identified in the Injun-5 electric field data. Electric field reversals occur on ~36% of auroral zone traversals, at about 70° to 80° invariant latitude, and at all local times. They have been identified at magnetically conjugate points in both hemispheres. Amplitudes are often greater than 30 mV m^{-1}, and occasionally greater than 100 mV m^{-1}. The latitude and structure of a reversal often change markedly on time scales less than 2 h. Electric potentials of greater than 40 keV are associated with reversals (Cauffman and Gurnett, 1971b). Reversals occur at the boundary of measurable intensities of >45 keV electrons and have been observed to be nearly (±100 km)

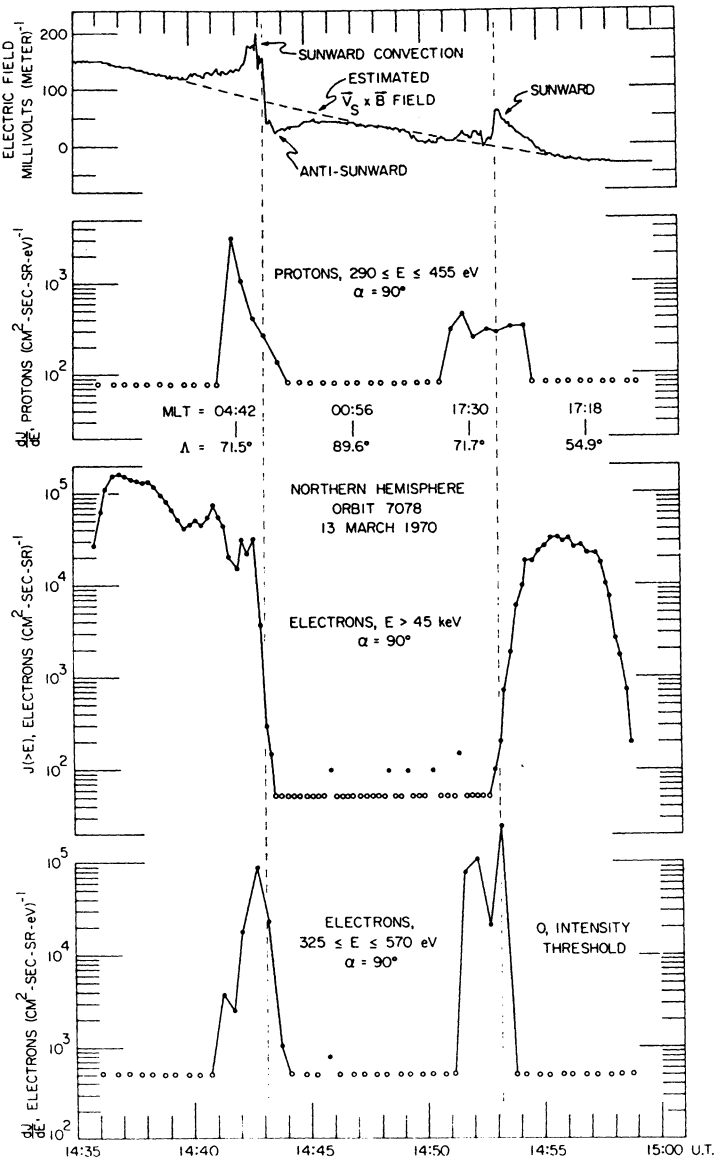

Fig. 21. (After Frank and Gurnett, 1971.) Simultaneous observations of proton and electron intensities at local pitch angle $\alpha = 90°$ and of electric fields for an Injun-5 northern polar pass in March, 1970.

coincident with inverted 'V' low-energy electron precipitation events. Generally the plasma convection velocities associated with reversals are directed east or west, with anti-sunward components at higher latitudes and sunward components at lower latitudes.

Maximum convection velocities generally occur near reversals and average ~1.5

km s^{-1}. Over the polar region above the auroral zone the convection velocity is usually small (generally not greater than 0.75 km s^{-1}, and sometimes less than 0.25 km s^{-1}) compared to convection velocities in the region of the reversal. Large scale anti-sunward convection across the magnetic poles with convection velocities exceeding 0.75 km s^{-1} is, however, occasionally observed.

B. OBSERVATIONS WITH OGO 6

An example of OGO-6 data taken at high latitudes in both hemispheres during one orbit is shown in Figure 22. The $\mathbf{V}_s \times \mathbf{B}$ field component due to the satellite velocity in a reference frame corotating with the earth has been subtracted from the data presented. The 5 to 10 mV m^{-1} offset observed in the Southern Hemisphere in Figure 22, as compared to the lack of offset in the Northern Hemisphere, is not well understood, but is systematic such that it can be approximately corrected by a baseline shift.

The most prominent feature of the OGO-6 data is the repeatable occurrence of electric fields corresponding to sunward convection at magnetic latitudes of $\sim 60°$ to $75°$ and anti-sunward convection at higher latitudes, as indicated in Figure 22. The maximum electric field intensities are observed in the sunward-convecting zone, equatorward of the electric reversal location, while poleward of the electric field reversal the electric field intensities are generally smaller (10–40 mV m^{-1}). The potential difference between the dawn and dusk electric field reversal locations is typically 40 to 80 kV. Figure 22 also illustrates the fact that more fluctuations in the electric fields are observed in the Southern Hemisphere than in the Northern Hemisphere. This is believed to be a seasonal effect, as the southern polar cap was in darkness in June, when these data were taken.

More subtle effects which have been found in the OGO-6 data include the following:

(1) In a number of cases the polar cap convection velocities observed at 2 to 5 h MLT are greater than those observed at 20–22 h MLT.

(2) The anti-sunward zones are often wider at dusk than at dawn local times.

(3) Numerous cases of 'non-typical' effects, such as large, rapid fluctuations (cf. Figure 23 at 07 54 UT) have been observed. These features are generally seen only in an isolated region of a given pass.

(4) The rapid fluctuations illustrated in Figure 23 were observed shortly after a negative bay which broke at 0749 UT, as shown by magnetograms at the bottom of the figure. The appearance of narrow zones of large electric field fluctuations seems to occur only during that part of a bay in which $|-\Delta H|$ is increasing. A single satellite measurement cannot resolve whether the fluctuations are spatial or temporal.

(5) While the electric fields observed bear no close relationship to magnetic activity, there is a statistical tendency for larger fields to occur when K_p is large. But there are numerous individual exceptions.

(6) There also exists a pronounced tendency for the boundaries associated with high latitude electric fields to be shifted equatorward and to occur at a wider range of latitudes during periods of magnetic activity. Figure 24 shows the shift in the locations of the maximum convection velocities observed in each of the 3 convection zones for a

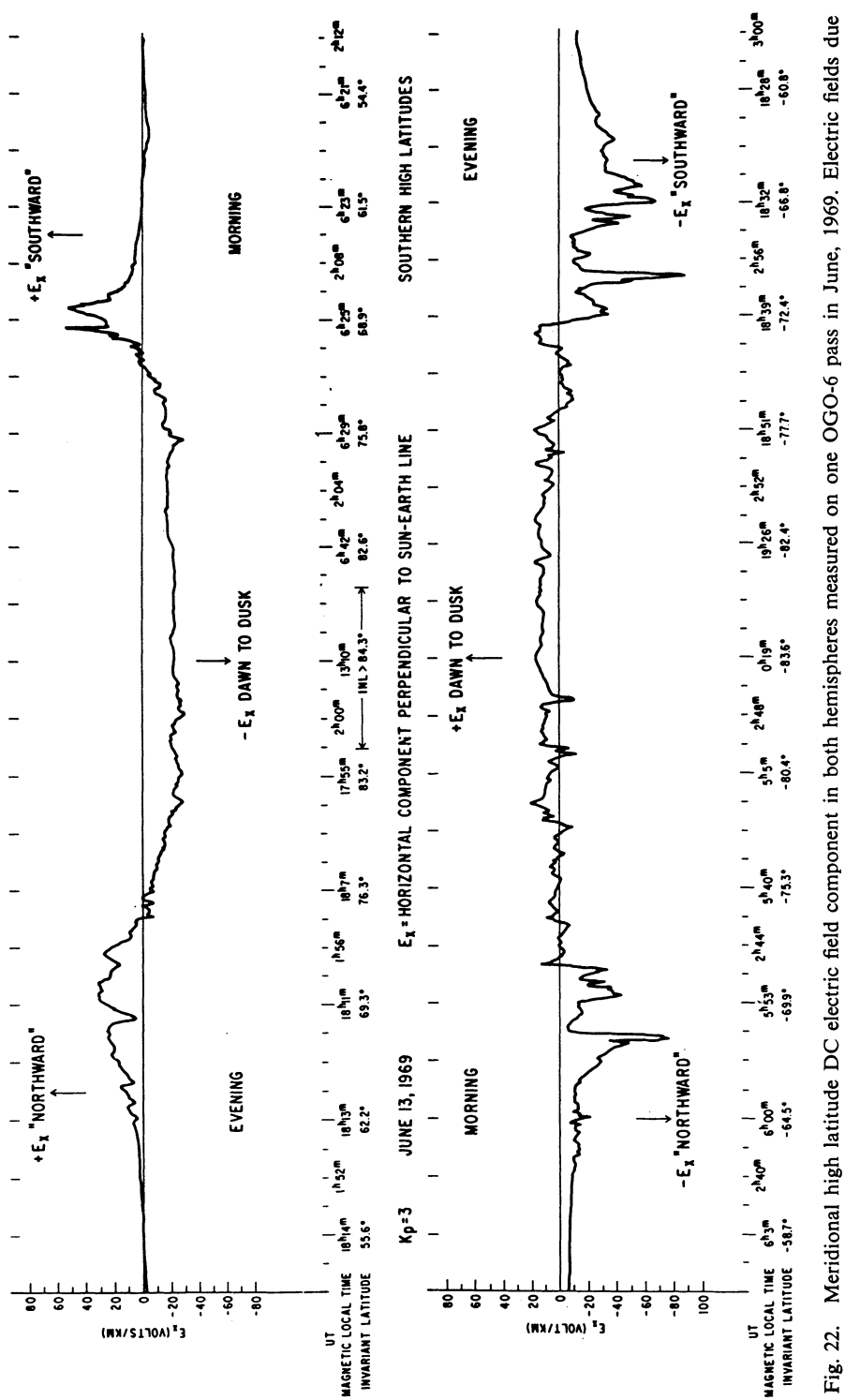

Fig. 22. Meridional high latitude DC electric field component in both hemispheres measured on one OGO-6 pass in June, 1969. Electric fields due to satellite motion and ionosphere corotation have been subtracted from the data shown. (Maynard, 1971, Figure 6.)

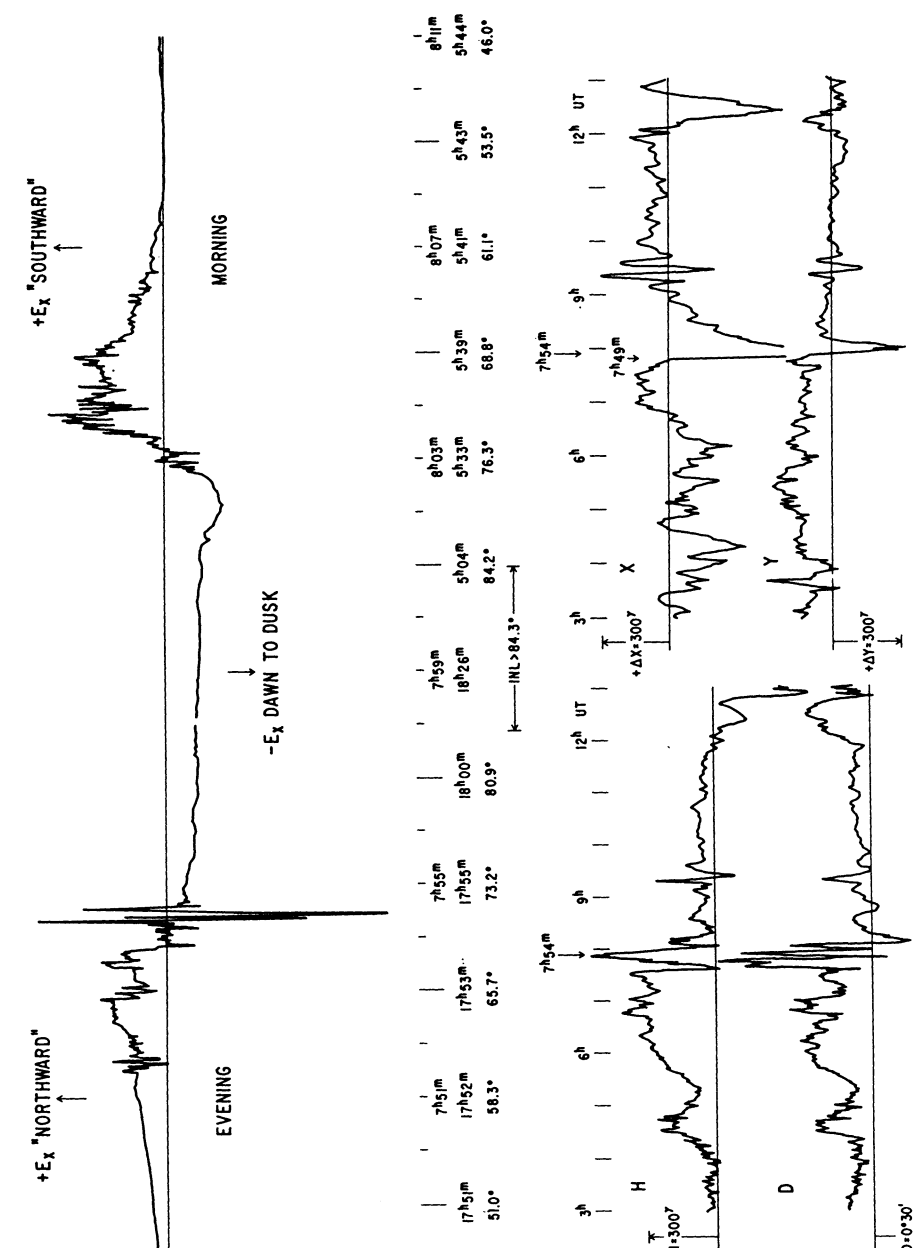

Fig. 23. Northern Hemisphere electric field component measured by OGO-6 shortly after the negative bay shown on the magnetograms from College and Churchill. (J. P. Heppner, talk presented at IUGG, Moscow, 1971.)

number of Northern Hemisphere passes. The reversal location also shifts equatorward.

It is apparently characteristic of the high latitude electric field data that many exceptions occur to virtually every generalization. Large temporal variations in the high latitude electric field signature occur even between successive polar passes. Dark-hemisphere electric fields are extraordinarily variable. Even in the sunlit hemisphere less than 50% of polar passes resemble in detail the 'typical' pass shown in Figure 22. This variability is illustrated by Figure 25, which shows 21 north polar orbits which pass within 5° latitude of the north magnetic dipole pole.

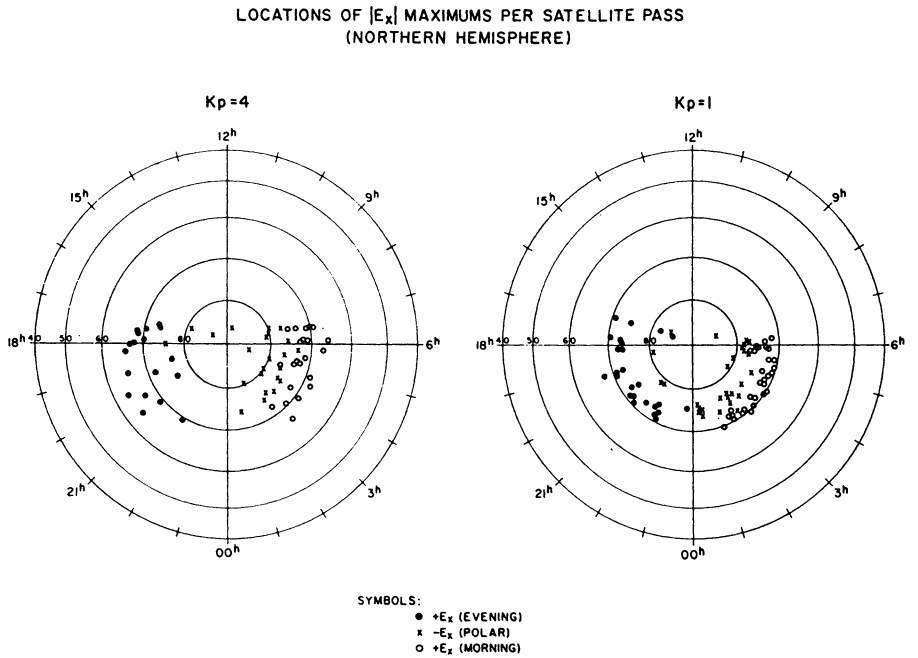

Fig. 24. Locations in invariant latitude and magnetic local time of the maximum-per-pass convection velocities measured by OGO 6 at periods of high and low magnetic activity, indexed by K_p. (J. P. Heppner, talk presented at IUGG, Moscow, 1971).

Figure 25 illustrates a wide variety of electric field configurations, varying from cases having nearly uniform anti-sunward convection over the polar cap region and almost complete dawn-dusk symmetry (orbits 64, 83, 97, and 121, for example) to cases with very low convection velocities over the polar cap and marked dawn-dusk asymmetries (orbits 150, 155, 184, 208, and 222, for example).

The initial OGO-6 results summarized in this paper have been reported by Maynard (1971) and Heppner (paper presented at IUGG, Moscow, August, 1971, to be published in *Planetary and Space Science*, 1972). Details of the OGO-6 electric field experiment and data were kindly provided by J. P. Heppner, T. L. Aggson, and N. C. Maynard (personal communications, 1971).

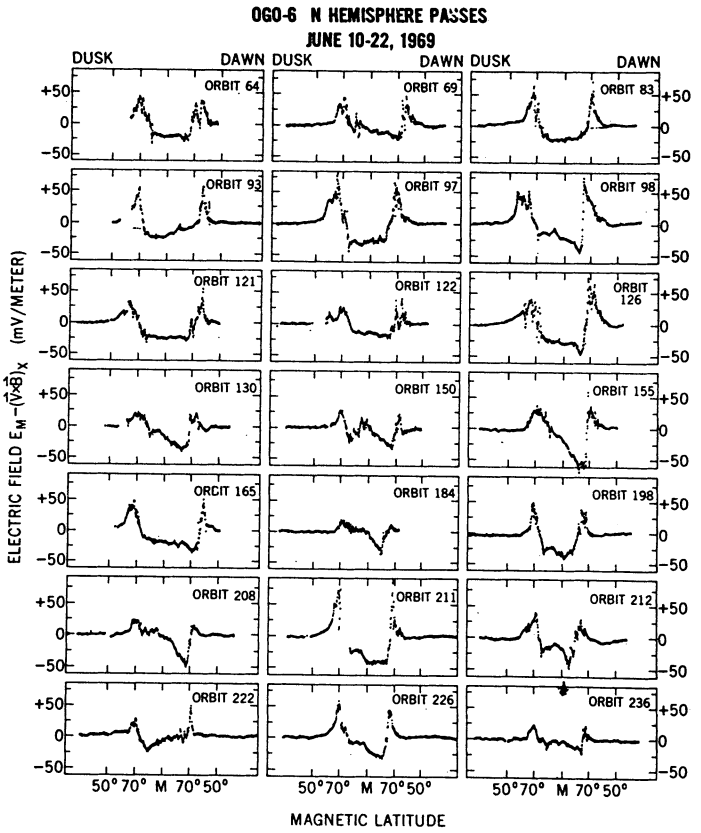

Fig. 25. Electric fields observed on 21 Northern Hemisphere passes with OGO 6 during June, 1969. The orbits were selected which passed within 5° magnetic latitude of the north dipole magnetic pole on the night side. (T. Aggson, personal communication).

6. Conclusions

A. COMPARISON OF SATELLITE MEASUREMENTS

Comparison of the Injun-5 electric field data in Figures 15, 17, and 21 with the OGO-6 data in Figure 25 illustrates the close similarity in the electric field observations by these two satellites. The convection diagrams of Figure 26 are intended to summarize the two extremes in the high latitude convection patterns observed by Injun-5 and OGO-6. It must be emphasized that these diagrams represent a gross simplification of the actual convection and that at any given time the convection pattern may differ markedly from these 'average' patterns. Major departures include

(1) the existence of multiple reversals, possibly indicative of a turbulent eddy-like convection pattern;

(2) the frequent disappearance of one or both of the convection zones associated with a reversal;

(3) marked dawn-dusk asymmetries in the convection pattern;

(4) temporal variations in the latitude of the reversal;

(5) the occurrence of anti-sunward convection velocities greater than 1.0 km s^{-1} across the entire polar cap, and

(6) variations in the sunward neutral point of the pattern by ± 2 h (as shown by the region of 'overlap' near local noon for the east–west convection in Figure 20).

The OGO-6 data substantiate the Injun-5 discovery of reversals in the electric field at auroral zone latitudes with sunward thermal plasma convection directions implied at latitudes below the reversal, and anti-sunward flow directions at higher latitudes. Both satellites also detect the same seasonal effect larger electric field fluctuations in the hemisphere where it is winter. Both agree that fields are highly variable and irregular and that no clear dependence of electric field magnitudes on magnetic activity has been established.

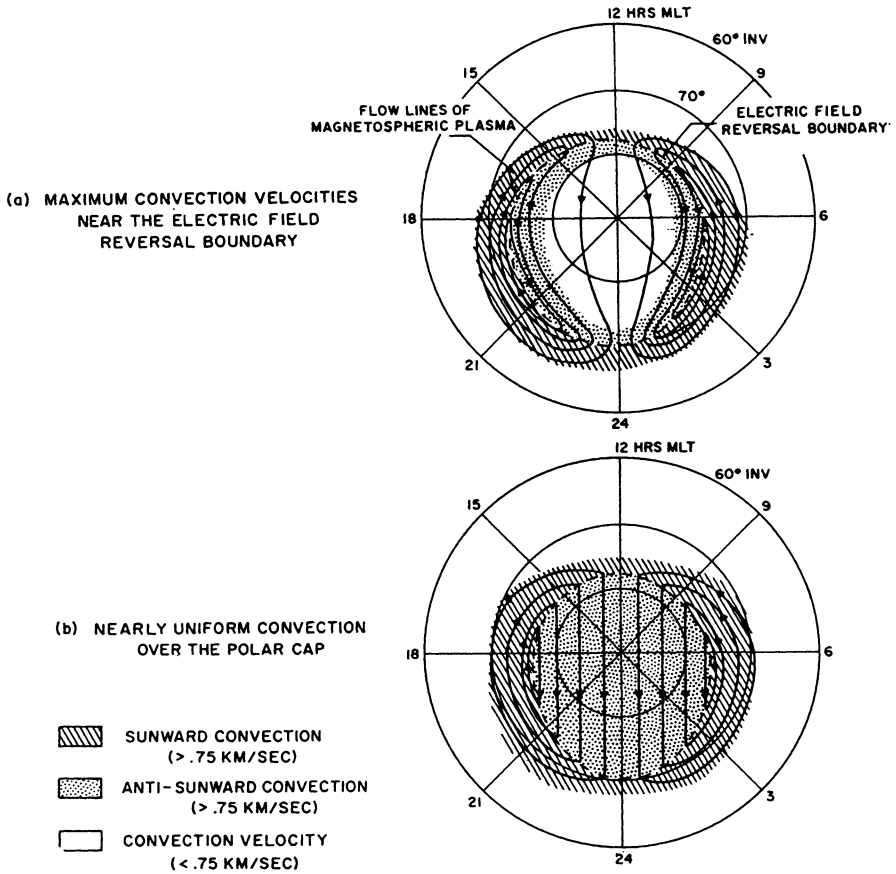

Fig. 26. Schematic diagram showing the average location and normal directions of > 0.75 km s^{-1} convection of thermal plasma at low altitudes in the magnetosphere as derived from measurements of electric fields with the Injun-5 and OGO-6 satellites. (a) and (b) represent two common convection configurations.

It was possible to perform an analysis of the probe system operation in orbit with Injun-5, because the satellite was spinning and because it carried experiments to measure electron density and sheath impedance. The results of this analysis support the validity of the theory of probe operation tested (see Sections 3 and 4). Injun-5 has the additional advantages of more complete local time coverage than OGO-6, and of measurements (at different times) of both components of $E_{\perp}$. Injun-5 results indicate that the phenomenon of electric field reversals does occur frequently even at noon local times.

OGO-6 has the advantages of greater sensitivity and of data uninterrupted by shadows and wake effects. OGO-6 data has revealed the existence of relatively uniform 10–40 mV m^{-1} electric fields at most times across the polar cap. These fields were usually not identifiable in the Injun-5 data, most of which were uncertain by ± 30 mV m^{-1}, although several cases of relatively uniform convection across the polar cap were observed with Injun-5 (see for example, Figures 15 and 17). OGO-6 has also been able to establish the existence of a small equatorward movement of the convection boundaries, associated with larger values of the magnetic index K_p.

The uncertainty which remains about the general configuration of high latitude electric fields $\geqslant 10$ mV m^{-1}, is confined to the noon and midnight regions, where OGO-6 does not measure the latitudinal component of convection, and Injun-5 cannot measure the <30 mV m^{-1} fields which may be expected to be important. However, as illustrated by Figures 18, 19, and 20, Injun-5 has established that electric field reversals do occur near 80° INV and noon local times. These reversals resemble in signature those observed near dawn and dusk, and have been shown to involve convection with primarily east–west components (Cauffman, 1971). However, it is open to question whether they form part of a 'usual' convection pattern. If they do, then the pattern must resemble that shown in Figure 26a. If not, the pattern must resemble that shown in Figure 26b. The flow lines in the latter diagram closely resemble the equipotential contours obtained from integrating OGO-6 data passes such as that shown in Figure 22, if the additional assumption of an azimuthal potential dependence proportional to sin φ is made (T. L. Aggson and J. Bose, private communication, 1971). The question is what happens in the 'usual' case; *observations corresponding to both patterns shown in Figure 26 have been made by each spacecraft.* (Cf. Figures 17 and 19 for Injun-5; Figure 25, orbits 150, 212, 83, and others, for OGO-6). More measurements are needed to resolve the matter, and it is possible that both patterns represent important modes of magnetosphere-solar wind interaction.

The midnight sector is also unclear from satellite data, although this region is amenable to study by barium release techniques, the results of which are summarized by Haerendel and Lust (1970). It is hoped that OGO-6 data from the Earth's shadow, when analyzed, will clarify the behavior of midnight electric fields.

B. COMPARISON WITH BARIUM CLOUD MEASUREMENTS

Haerendel and Lust (1970) summarize recent results of measurements of plasma convection by the barium cloud drift technique. The requirement of twilight conditions

restricts barium cloud measurements to invariant latitudes generally below 70° and primarily to the midnight sector. At local times near dawn, eastward drifts are observed, and near dusk, westward drifts. These directions are entirely consistent with the 'sunward' convection reported in this paper at dawn and dusk at comparable latitudes. Several cases have been reported of high latitude barium clouds which reverse their east–west drift directions indicating that the clouds crossed an electric field reversal of the type observed with Injun-5 and OGO-6. The magnitudes of convection electric fields observed by Injun-5 and OGO-6 are consistent with those quoted by Wescott *et al.* (1969), who report intensities of 10–130 mV m^{-1}. These authors also report that large irregularities in the electric field exist most of the time.

C. COMPARISON WITH MAGNETOSPHERIC AND AURORAL MODELS

High latitude convection is intimately tied to the topology of the outer magnetosphere and the geomagnetic tail, and probably to events and magnetic field directions in the solar wind as well. Electric field reversals and the related convection patterns observed have important implications on the magnetic field topology involved in the solar wind/magnetosphere interaction. The observation of antisunward convection on the poleward side of the electric field reversal and sunward convection on the equatorward side, and the coincidence of the electric field reversal with the high latitude termination of measurable intensities of $E > 45$ keV electrons suggests that the electric field reversal is related to the boundary between 'open' field lines on the poleward side of the electric field reversal which connect into the solar wind and 'closed' field lines on the equatorward side of the electric field reversal which connect to the opposite hemisphere without entering the solar wind (Frank and Gurnett, 1971). The observed convection velocities on the poleward side of the electric field reversal indicate that the polar cap field lines do not freely connect to the solar wind, as implied by Dungey's (1961) model, but rather a physical limit to the reconnection rate exists as discussed by Petschek (1964). Large magnitude (> 0.75 km s^{-1}) anti-sunward convection over the polar cap regions are infrequently observed and the largest convection velocities are observed near the electric field reversal. An observational model incorporating the essential features of the observed convection has been discussed by Frank (1971) and Frank and Gurnett (1971). The observation of the largest convection velocities near the electric field reversal is also consistent with the Axford and Hines (1961) model, in which Earth's 'closed' field lines are distorted and set into convection motion by the solar wind through viscous interaction at the magnetopause. Electric field measurements at the magnetopause, which are made by IMP I, are in progress to resolve the question of reconnection versus viscous interaction at that boundary. Convection patterns similar to those observed by Injun-5 have also been predicted by the model of Hill and Dessler (1971). The magnetic substorm two-dimensional equivalent current systems derived by Nishida (1967), Heppner (1969), Wescott *et al.* (1969), and others, do predict the observed reversals and the directions of convection, but are difficult to relate to the observed electric fields because of the uncertainty in the ionospheric conductivities.

D. GOALS AND RECOMMENDATIONS FOR FUTURE EXPERIMENTS

Clearly, satellite electric field measurements have provided valuable new information on magnetospheric convection processes. However, many improvements in the experimental techniques can be made. What are needed are (1) more sensitive measurements, (2) measurements with two or more antennas in order to obtain the instantaneous vector direction of the convection velocity, (3) sensitive measurements of parallel electric fields at all altitudes, (4) simultaneous measurements of electric fields at slightly separated points in space to separate spatial and temporal variations, and (5) investigations of the electric fields at the plasmapause, magnetopause, and polar cusp regions in particular. The IMP-I mission is expected to make significant contributions with regard to item (5). Economic hurdles notwithstanding, these goals are difficult to achieve, as attested by the magnitude and diversity of the experimental difficulties discussed in Section 4B. At high altitudes additional problems, which have not been discussed, occur due to increased spacecraft sheath size, greatly increased ratio of photocurrents to ram currents, and mechanical problems associated with the long antenna lengths required.

We summarize below some of the most important practical considerations which we feel are important to obtain reliable electric field measurements.

(1) Symmetry for double-probe systems is of paramount importance. Stub booms should be added to give the probes translational symmetry, as suggested by Fahleson (1967). Stub booms, which could not be flown on Injun-5 because of mechanical constraints, would have eliminated the boom shadowing problems we encountered. Efforts should be made to achieve identical photo-emission properties for the surfaces of the two spheres (see Fahleson *et al.*, 1970), and to ensure that the surfaces stay clean during launch. The spheres must be as similar as possible electrically, particularly with respect to having equal differential amplifier input resistances in each branch. The probe surfaces should have equal and uniform work functions.

(2) It is essential that the input impedance of the differential amplifier be very much higher than the sheath impedances encountered anywhere in the satellite orbit.

(3) Accurate knowledge of satellite attitude is critical for calculating the component of the $\mathbf{V}_s \times \mathbf{B}$ field parallel to the antenna axis and determining shadowing conditions.

(4) The measurement of plasma sheath impedance by Injun-5 proved to be a valuable adjunct to the electric field measurement, and quantitative error analysis would not have been possible without it. We suggest that future missions by other experimenters would also be improved by including an impedance measurement.

(5) Simultaneous measurements of plasma parameters, such as electron number density and temperature, are invaluable in evaluating the performance of the electric antenna, as well as for investigating the complex phenomena, such as aurorae, occurring in the magnetosphere.

(6) The *only way* to make reliable double-probe measurements of electric fields at high altitudes in the magnetosphere is to use long enough booms to measure fields in regions of space which are undisturbed by the Debye or photo-sheaths of the space-

craft itself. The use of long, flexible, centrifugally deployed wire antennas, possibly several hundred meters in length, deserves serious consideration.

Acknowledgements

We wish to thank Dr James A. Van Allen for his support and guidance on the Injun-5 project. We are indebted to Drs J. P. Heppner, T. L. Aggson, and N. C. Maynard of Goddard Space Flight Center for cooperation and generosity in providing and discussing results from the OGO-6 satellite. Dr Rita Sagalyn of Air Force Cambridge Research Laboratories kindly provided data on electron number densities measured with Injun-5.

This research was supported in part by the National Aeronautics and Space Administration under contracts NAS5-10625, NAS1-8141, NAS1-8144 (f), NAS1-8150 (f), and NGL-16-001-043(97); and by the Office of Naval Research under contract N00014-68-A-0196-0003.

Part of this paper was prepared while one author (DPC) was a NAS research associate in the Magnetic and Electric Fields Branch, Code 645, NASA/Goddard Space Flight Center, Greenbelt, Maryland 20771.

References

Aggson, T. A.: 1966, 'A Proposal for Tri-Axial Electric Field Measurements on IMP Spacecraft H, I, and J', NASA-Goddard Space Flight Center preprint.

Aggson, T. A.: 1969, in B. M. McCormac and A. Omholt (eds.), *Atmospheric Emissions*, Van Nostrand-Reinhold, New York, p. 305.

Aggson, T. A. and Heppener, J. P.: 1964, 'A Proposal for Electric Field Measurements on ATS 1', NASA-Goddard Space Flight Center preprint (updated 1965).

Akasofu, S. I. and Meng, C. I.: 1969, *J. Geophys. Res.* **74**, 293.

Alfvèn, H.: 1967, *Space Sci. Rev.* **7**, 140.

Axford, W. I.: 1969, *Rev. Geophys.* **7**, 421.

Axford, W. I. and Hines, C. O.: 1961, *Can. J. Phys.* **39**, 1433.

Block, L. P. and Fälthammar, C.-G.: 1968, *J. Geophys. Res.* **73**, 4807.

Bonnevier, B., Bostrom, R., and Rostocker, G.: 1970, *J. Geophys. Res.* **75**, 107.

Bostrom, R.: 1967, in B. M. McCormac (ed.), *Aurora and Airglow*, Reinhold Book Corp., New York, p. 293.

Cain, J. C., Hendricks, S. J., Langel, R. A., and Hudson, V. W.: 1967, *J. Geomagn. Geoelec.* **19**, 335.

Carlqvist, P. and Bostrom, R.: 1970, *J. Geophys. Res.* **75**, 7140.

Carpenter, D. L.: 1970, *J. Geophys. Res.* **75**, 3837.

Cauffman, D.: 1971, 'A Satellite Study of DC Electric Field Reversals in the Magnetosphere', Univ. of Iowa 71-15 (University of Iowa Research Report).

Cauffman, D. and Gurnett, D. A.: 1971a, *J. Geophys. Res.* **76**, 6014.

Cauffman, D. and Gurnett, D. A.: 1971b, 'Catalogue of DC Electric Field Reversals Observed with the Injun-5 Satellite', Univ. of Iowa 71-10 (University of Iowa Research Report).

Dungey, J. W.: 1961, *Phys. Rev. Letters* **6**, 47.

Fahleson, U. V.: 1967, *Space. Sci. Rev.* **7**, 238.

Fahleson, U. V., Kelley, M. C., and Mozer, F. S.: 1970, *Planetary Space Sci.* **18**, 1551.

Feldstein, Y. I.: 1966, *Planetary Space Sci.* **14**, 121.

Foppl, H., Haerendel, G., Haser, L., Lust, R., Melzner, F., Meyer, B., Neuss, H., Rabben, H., Rieger, E., Stocker, H., and Stoffregen, W.: 1968, *J. Geophys. Res.* **73**, 21.

Frank, L. A.: 1971, *J. Geophys. Res.* **76**, 5202.

Frank, L. A.: 1971, *J. Geophys. Res.* **76**, 2512.
Frank, L. A. and Ackerson, K. L.: 1971, *J. Geophys. Res.* **76**, 3612.
Frank, L. A. and Gurnett, D. A.: 1971, *J. Geophys. Res.* **76**, 6829.
Frank, L. A., Stanley, W. W., Gabel, R. H., Enemark, D. C., Randall, R. F., and Henderson, N. K.: 1966, 'Technical Description of LEPEDEA Instrumentation (Injun-5)', Univ. of Iowa 66-31 (University of Iowa Research Report).
Gurnett, D. A.: 1970, in B. M. McCormac (ed.), *Particles and Fields in the Magnetosphere*, D. Reidel Publishing Company, Dordrecht, Holland, p. 239.
Gurnett, D. A., Pfeiffer, G. W., Anderson, R. R., Mosier, S. R., and Cauffman, D. P.: 1969, *J. Geophys. Res.* **74**, 4631.
Haerendel, G.: 1970, 'Electric Fields and Their Effects in the Ionosphere', Research Report, MPI, PAE-Extraterr. 44/70, Max-Planck-Institut für Physik und Astrophysik, München, July.
Haerendel, G. and Lust, R.: 1970, in B. M. McCormac (ed.), *Particles and Fields in the Magnetosphere*, D. Reidel Publishing Company, Dordrecht, Holland, p. 213.
Haerendel, G., Lust, R., and Reiger, E.: 1967, *Planetary Space Sci.* **15**, 1.
Heppner, J. P.: 1969, in B. M. McCormac and A. Omholt (eds.), *Atmospheric Emissions*, Van Nostrand Reinhold, New York, p. 251.
Hill, T. W. and Dessler, A. J.: 1971, 'Plasma-Sheet Structure and the Onset of Magnetospheric Substorms, *J. Geophys. Res.*, in press.
Kasha, Michael A.: 1969, *The Ionosphere and Its Interaction with Satellites*, Gordon and Breach, New York.
Maynard, N. C.: 1972, 'Electric Fields in the Ionosphere and Magnetosphere', NASA-Goddard Space Flight Center preprint X-645-71-231 (1971), to be published in K. Folkestad (ed.), *Proceedings of the Advanced Study Institute on Magnetosphere-Ionosphere Interaction, April 14–23, 1971*, Univ. of Oslo Press, Norway, in press.
Maynard, N. C. and Heppner, J. P.: 1970, in B. M. McCormac (ed.), *Particles and Fields in the Magnetosphere*, D. Reidel Publishing Company, Dordrecht, Holland, p. 247.
Mende, S. B.: 1968, *J. Geophys. Res.* **73**, 991.
Mott-Smith, H. M. and Langmuir, I.: 1926, *Phys. Rev.* **28**, 727.
Mozer, F. S. and Bruston, P.: 1967, *J. Geophys. Res.* **72**, 1109.
Mozer, F. S. and Serlin, R.: 1969, *J. Geophys. Res.* **74**, 4739.
Nishida, A.: 1967, *J. Geophys. Res.* **72**, 6051.
Petschek, H. E.: 1964, in W. N. Hess (ed.), *Proc. AAS-NASA Symp. on the Physics of Solar Flares*, NASA SP-50, Washington, D.C., p. 425.
Piddington, J. H.: 1962, *Planetary Space Sci.* **9**, 947.
Potter, W. E.: 1970, *J. Geophys. Res.* **75**, 5415.
Van Allen, J. A.: 1970, *J. Geophys. Res.* **75**, 29.
Wescott, E. M., Stolarik, J. D., and Heppner, J. P.: 1969, *J. Geophys. Res.* **74**, 3469.
Wildman, P. J. L.: 1965, *J. Atmospheric Terrest. Phys.* **27**, 417.
Woodman, R. F. and Hagfors, T.: 1969, *J. Geophys. Res.* **74**, 1205.